



AFRL-OSR-VA-TR-2014-0074

FINITE ELEMENT ANALYSIS OF EUTECTIC STRUCTURES

Alp Sehirlioglu
CASE WESTERN RESERVE UNIV CLEVELAND OH

03/12/2014
Final Report

DISTRIBUTION A: Distribution approved for public release.

Air Force Research Laboratory
AF Office Of Scientific Research (AFOSR)/ RTD
Arlington, Virginia 22203
Air Force Materiel Command

REPORT DOCUMENTATION PAGE				<i>Form Approved</i> OMB No. 0704-0188	
<small>Public reporting burden for this collection of information is estimated to average 1 hour per response, including the time for reviewing instructions, searching existing data sources, gathering and maintaining the data needed, and completing and reviewing this collection of information. Send comments regarding this burden estimate or any other aspect of this collection of information, including suggestions for reducing this burden to Department of Defense, Washington Headquarters Services, Directorate for Information Operations and Reports (0704-0188), 1215 Jefferson Davis Highway, Suite 1204, Arlington, VA 22202-4302. Respondents should be aware that notwithstanding any other provision of law, no person shall be subject to any penalty for failing to comply with a collection of information if it does not display a currently valid OMB control number. PLEASE DO NOT RETURN YOUR FORM TO THE ABOVE ADDRESS.</small>					
1. REPORT DATE (DD-MM-YYYY)		2. REPORT TYPE		3. DATES COVERED (From - To)	
4. TITLE AND SUBTITLE				5a. CONTRACT NUMBER	
				5b. GRANT NUMBER	
				5c. PROGRAM ELEMENT NUMBER	
6. AUTHOR(S)				5d. PROJECT NUMBER	
				5e. TASK NUMBER	
				5f. WORK UNIT NUMBER	
7. PERFORMING ORGANIZATION NAME(S) AND ADDRESS(ES)				8. PERFORMING ORGANIZATION REPORT NUMBER	
9. SPONSORING / MONITORING AGENCY NAME(S) AND ADDRESS(ES)				10. SPONSOR/MONITOR'S ACRONYM(S)	
				11. SPONSOR/MONITOR'S REPORT NUMBER(S)	
12. DISTRIBUTION / AVAILABILITY STATEMENT					
13. SUPPLEMENTARY NOTES					
14. ABSTRACT					
15. SUBJECT TERMS					
16. SECURITY CLASSIFICATION OF:			17. LIMITATION OF ABSTRACT	18. NUMBER OF PAGES	19a. NAME OF RESPONSIBLE PERSON
a. REPORT	b. ABSTRACT	c. THIS PAGE			19b. TELEPHONE NUMBER (include area code)

**FINAL REPORT:
2009 through 2013**

For the Grant

Finite Element Analysis of Eutectic Structures:

FA9550-09-1-0312

Submitted to

Air Force Office of Scientific Research

By

Dr. Alp Sehirlioglu (Assistant Professor)

Dr. Ali Sayir (Research Associate Professor)

CASE WESTERN RESERVE UNIVERSITY

Thermoelectric Properties of WSi₂-Si_xGe_{1-x} Composites

Thermoelectric properties of the W/Si/Ge alloy system have been investigated with varying concentration levels of germanium and tungsten. The alloys were fabricated by directional solidification with the Bridgman method using boron nitride and fused silica crucibles. The effect of crucible contamination was investigated and found to result in doping the system to suitable levels for thermoelectric applications. The system has been demonstrated as a suitable high temperature p-type thermoelectric material exhibiting high power factors, $>3,000 \mu\text{W}/\text{m}\cdot\text{K}^2$. Seebeck coefficients of the system are on the order of $+300 \mu\text{V}/\text{K}$ and electrical conductivities of $2.8 \times 10^4 \text{ S}/\text{m}$ at the optimum operating temperature. The best composition, 0.9 at% W/9.3 at% Ge, achieved a figure of merit comparable to RTG values over the temperature range of interest. The results suggest that W addition can reduce the use of expensive Ge component of the alloy. Reported are the details of processing conditions, microstructure development, and temperature dependent thermoelectric properties. The material system was stable at the temperatures required for NASA's radioisotope thermoelectric generators.

1. Introduction

Energy consumption is growing at a staggering pace due to global population growth and economic development. Global energy consumption is approaching 50 TW/yr, new power generation strategies are needed to meet the demand. Waste heat is an abundant source that is under-utilized as an energy resource with no additional greenhouse gas emissions. Thermoelectric (TE) technology provides direct conversion of heat to electric power by utilizing the coupled transport of thermal and electrical energy. Space exploration has proven that thermoelectric power generation is highly reliable and exhibits long term operational life [1]. The development of thermoelectric materials with higher conversion efficiencies provides the pathway to expand TE technology into commercial markets such as waste heat recovery. The thermoelectric conversion efficiency of a material is the product of the Carnot efficiency and material conversion efficiency. The conversion efficiency of a thermoelectric material is evaluated by the dimensionless figure of merit (ZT):

$$ZT = \frac{\sigma \alpha^2}{\lambda} T \quad (1)$$

where α is the Seebeck coefficient, σ is the electrical conductivity, λ is the total thermal conductivity, and T is the absolute temperature. Total thermal conductivity λ includes heat conduction by both the lattice and charge carriers. The inter-dependency of the material properties (α , σ , λ) has plagued the development of high efficiency TE materials. Historically, ZT improvements have been achieved by alloying, which causes strong phonon scattering. Reduction in thermal conductivity achieved by alloying is usually offset by deterioration in electrical transport, limiting ZT enhancement.

Technology advancement has led to higher ZT by decoupling TE property inter-dependency via microstructural engineering, which provides a method to control phonon transport by scattering dominant phonon wavelengths without detrimental effect on electrical transport. For high temperature applications, the majority of phonons are most effectively scattered by inclusions at

the nano-scale as a result of greater interface area per unit volume of the inclusions as well as enhanced distribution of the inclusions in the matrix. Such nano-inclusions have been effective in enhancing ZT. Nano-inclusions can reduce thermal conductivity below the “alloy limit”, e.g., $\text{In}_{0.53}\text{Ga}_{0.47}\text{As}$ containing semi-metallic ErAs nanoparticles [2]. Additionally, semi-metallic nanoparticles enhance electrical properties as demonstrated by ErSb particles in a GaSb matrix and ErAs particles in InGaAlAs [2]. Similarly for the $\text{Si}_x\text{Ge}_{1-x}$ system nano-particle in $\text{Si}_x\text{Ge}_{1-x}$ have been investigated both theoretically [12,39] and experimentally for the $\text{Si}_{80}\text{Ge}_{20}\text{-CrSi}_2$ system [38].

Directional solidification of off-eutectic and eutectic-compositions is well-known to yield self-assembled microstructures that are non-achievable by solid state sintering. The microstructure can exhibit many geometrical forms: dendritic, lamellar, and rods. The self-assembled structure can be controlled or engineered by process variables and material volume fraction. Additionally, formation of low energy coherent interfaces and textured/oriented microstructures often occur by directional solidification. Coherent interfaces may reduce electron scattering and enhance Seebeck coefficient. Enhanced ZT has been reported for oriented $\text{Bi}_{0.5}\text{Sb}_{1.5}\text{Te}_3$ [4]. Solidification techniques have been reported for TE systems of PbTe– Sb_2Te_3 [5], PbTe-Si [6], $\text{Pb}_{1-x}\text{Sn}_x\text{Te-PbS}$ [7], $\text{AgPb}_m\text{SbTe}_{2-m}$ [8], Ag-Pb-Te [9], and Si-Ge [16,20,25,26,28,32,36].

Due to their abundance, low cost and low toxicity, metal silicides have been investigated as potential high temperature TE materials [10]. A recent work that has focused on Mg-Si alloys achieved $\text{ZT} > 1$ [11]. Additional interest has arisen for Si-Ge composites from modeling work. Computations indicate that a strong reduction in thermal conductivity can be achieved in Si-Ge alloys containing metal silicide nanoparticles [12]. We have investigated directional solidification of a number of M-Si and M-Ge-Si (where M = Ti, Mo, W, Cr, Zr, Ta, V) systems [13]. Directional solidification in these systems does not yield an alloy containing nanoparticles. However, the Si-Ge-W system exhibits good TE properties.

Investigation centered on minor addition of W (≤ 3 at%) to $\text{Si}_x\text{Ge}_{1-x}$ alloys. The W addition forms metallic WSi_2 inclusions with a melting point of 2437 K. Metallic inclusions in thermoelectric materials are an untraditional approach for TE composites. The work shows that the addition of WSi_2 can reduce Ge content by 50% for optimal thermoelectric performance.

2. Experimental Procedure

Directional solidification was accomplished using the vertical Bridgman method. Starting materials for ingot preparation were ~5 mm silicon granules (Cerac, Milwaukee, WI, $\geq 99.9\%$), 100 mesh germanium powder (Alfa Aesar, Ward Hill, MA, $\geq 99.9\%$) and 100 mesh tungsten powder (Alfa Aesar, $\geq 99.9\%$). Alloys were melted in a helium atmosphere in a graphite resistance heated furnace (Thermal Technology LLC, Santa Rosa, CA). Temperature was controlled by an optical pyrometer. Boron nitride (BN) (Momentive Performance Materials, Albany, NY) and fused silica (SiO_2) (Momentive Performance Materials, Albany, NY) crucibles were used. Calcium chloride (CaCl_2) was added to the SiO_2 crucible as an interfacial material between crucible and melt; eliminating mechanical failure of the crucible during sample cooling [14]. Ingots were prepared through two solidification runs. The first solidification served to consolidate the raw material into an ingot. Processing temperatures ranged from 1798 K to 1973 K with soak times of 1-3 hours. After the first solidification, additional raw material was added to achieve a 30-40 g sample with approximate dimensions of 20 mm in length and 22 mm in

diameter. The second solidification included directional solidification with a pull rate of 200 mm/hr over the temperature gradient that naturally exists in the furnace. The measured temperature gradient was 8.5 K/mm. It should be noted that zone leveling was not performed on the specimens presented in this work; rather the specimens were investigated as obtained at the completion of the second solidification run.

Table 1: Nominal compositions of the specimens studied

#	Si (at%)	Ge (at%)	W (at%)	Si (wt%)	Ge (wt%)	W (wt%)
1	99.2	0.0	0.8	95	0	5
2	94.8	4.3	0.9	85	10	5
3	89.8	9.3	0.9	75	20	5
4	84.3	14.9	0.8	66	30	4
5	82.4	14.6	3.0	59	27	14
6	77.6	19.4	3.0	53	34	13
7	72.7	24.3	3.0	47	40	13

Measurement of the Seebeck coefficient and electrical conductivity were made simultaneously using a ZEM-3 Seebeck Coefficient/ Electrical Resistance Measurement System (Ulvac Technologies, Methuen, MA). The system performs a four-point electrical conductivity measurement while simultaneously measuring the Seebeck coefficient and temperature differential using two type-K thermocouples. Seebeck coefficient of the type-K thermocouples was automatically compensated by the software. A temperature gradient was established across the specimen by a platinum heater mounted in the lower support arm. Specimen dimensions were 4x4x18 mm. Measurement was performed in a helium atmosphere at 85 Torr, a temperature range of 373 to 1273 K and thermal gradients ranging from 0.4 to 0.7 K/mm were employed. A temperature stability of ± 0.25 K was maintained over the course of the measurement at each temperature step.

The thermal conductivity (λ) of specimens was calculated from thermal diffusivity (D), heat capacity (C_p) and density (ρ): by the relation $\lambda = \rho DC_p$. Thermal data was measured in the temperature range of 373 to 1273 K by the laser flash method (Anter Flashline 5000, Anter Corporation, Pittsburgh, PA); density was determined by sample mass and geometric dimensions. Measurements followed ASTM E1461. Pyroceram was used as the standard for each measurement to calculate specific heat of samples, detector was liquid nitrogen cooled InSb. Samples were cut from the ingots with thickness of 2-3 mm and diameter of 12.5 mm. Samples were platinum coated with <1 μm thickness by physical vapor deposition (Lesker PVD-75, Kurt J. Lesker Corporation, Jefferson Hills, PA); ensuring an opaque surface to laser irradiation. Platinum thickness is negligible when compared to the specimen thickness, therefore is not believed to alter thermal measurements significantly. Specimens were also coated with carbon

paint in accordance with standard flash method to ensure a consistent repeatable emissivity. Three measurements were taken for each sample per temperature and the results were averaged. The time–temperature curves were analyzed by the method of Clark and Taylor [15].

Due to ingot physical constraints, samples obtained for thermal conductivity and electrical measurement could not be obtained with the same orientation. Thermal conductivity samples coincide with the axial direction of the ingot, while electrical samples were obtained in the radial direction (perpendicular to pull direction). Microstructural investigation indicated isotropic structures in both axial and radial directions, diminishing the effect of orientation.

Microstructural characterization was performed with a Hitachi S-4700 field emission scanning electron microscope (Hitachi High Technologies, Gaithersburg, MD) equipped with energy dispersive X-ray spectroscopy (EDS) (EDAX, Mahwah, NJ). Other characterization included inductively coupled plasma mass spectroscopy (ICP) with a Varian Vista Pro (Varian, Palo Alto, CA), X-ray diffraction (XRD) on a D-8 Advance (Bruker, Billerica, MA), and oxygen nitrogen determination with a TC-436 (Leco, St. Joseph, MI).

3. Results and Discussion

3.1. Microstructure

All specimens showed similar microstructures, an example of which is shown in the back-scattered SEM micrograph in Figure 1 (taken at 15 kV) for an alloy containing 0.9 at% W and 9.3 at% Ge (Sample 3 in Table 1). Chemical mapping by EDS is also added to show the Si, Ge and W distribution in the microstructure. Large 10 to 100 μm faceted precipitates were observed in the matrix. Chemical map shows that the entire W content is in the precipitates which were identified as WSi_2 via XRD (Figure 2). Determination of crystal growth habits was not integral to this investigation. Solidified microstructures are irregular with very little indication for preferred ordering of the WSi_2 phase. The solidification parameters inevitably lead to a considerable amount of micro-segregation resulting in a non-uniform matrix with varying Si to Ge ratios as observed both in the elemental maps and in the backscattered image of the matrix in Figure 1. Although Si and Ge exhibit complete solid state solubility, it is well known that solidification is non-congruent with the melt [16]. Local Ge content was determined through standardless EDAX ZAF quantification. For sample 3, with a nominal 9.3 at% Ge content, a range of 6.4 to 15.6 at% Ge was measured. Bulk ICP measurements on the same sample calculate an average of 8.8 at% Ge. The Ge rich areas of the samples tend to coincide near or surrounding the tungsten silicide precipitates. In the micrograph shown (Figure 1) the areas with the highest Ge content are either adjacent to, or enclosed by the silicide precipitates. This is likely due to a Ge rich boundary layer that forms as Ge was rejected from the WSi_2 precipitates during crystallization. This silicide driven micro-segregation may help explain some of the composite properties introduced later in section 3.3 Thermoelectric properties. Figure 2 shows the characteristic powder XRD of sample 3, the $\text{Si}_{89.8}\text{Ge}_{9.3}\text{W}_{0.9}$ system, in comparison to a comparable melt derived $\text{Si}_{90}\text{Ge}_{10}$ specimen. Both samples have the same Si/Ge ratio and were solidified under identical conditions. Additional peaks present in the W containing sample correspond to tetragonal WSi_2 precipitates. The XRD patterns shown in Figure 2 are typical for all the W/Si/Ge compositions investigated.

Rietveld refinement was performed using Topas (Bruker) software. The WSi_2 phase was analyzed over a 2Θ range of 30° to 45° to exclude reflections from the $\text{Si}_x\text{Ge}_{1-x}$ phase. Data was acquired in a Bragg-Brentano configuration with 300mm radius, 4° sollers, at a rate of 3.5° per min. The model was fit with an Rexp value of 4.51 and GOF value of 1.27, lattice parameters and Lorentzian crystallite domain size were the parameters of study in the model. Results show crystallite domain size of 238 nm with tetragonal lattice parameters of $a=b=0.321$ nm and $c=0.783$ nm. The measured lattice parameters match the reported values for WSi_2 , $a=b=0.32138$ nm and $c=0.78299$ nm [17]. XRD results indicate that the large WSi_2 precipitates are polycrystalline. The $\text{Si}_x\text{Ge}_{1-x}$ matrix could not be accurately represented by the model, making quantitative phase analysis impractical. Model failure arises from compositional peak broadening due to the non-uniform Ge concentration. Crystallite size or lattice strain could not be deconvoluted from the XRD data for the Si/Ge matrix. A more advanced fitting technique must be employed in order to account for the peak broadening due to the range of alloying present, such a model has been presented in the work of Leineweber et al. [19]. The average matrix lattice parameter from the $\text{Si}_x\text{Ge}_{1-x}$ peak positions revealed predominate cubic lattice parameter of 0.544 nm for both compositions. This $\text{Si}_x\text{Ge}_{1-x}$ lattice parameter is in good agreement with the work of Dismukes et al. [20], lattice parameter for $\text{Si}_{90}\text{Ge}_{10}$ composition is 0.545 nm. The introduction of tungsten into the system had no observable effect on the lattice spacing of the bulk matrix, suggesting that little to no tungsten is soluble into the $\text{Si}_x\text{Ge}_{1-x}$ matrix.

Jackson and Hunt [21] developed a method to predict eutectic microstructures based upon entropy of fusion. Theory states that phases with high entropy of formation (ΔS_f) form faceted interfaces when $\Delta S_f/R > 2$ (where R =gas constant). The entropies of formation of interest in this system are roughly $\Delta S_{\text{Si}} \sim 30$ J/K-mol, $\Delta S_{\text{Ge}} \sim 30$ J/K-mol [22], and $\Delta S_{\text{WSi}_2} \sim 18$ J/K-mol [23]. The dimensionless $\Delta S_f/R$ values are >2 : Si and Ge exhibiting $\Delta S_f/R$ of 3.6 and WSi_2 exhibits $\Delta S_f/R$ of 2.1 favoring faceted precipitates. Growth direction of the faceted phase is determined by the specific crystallographic orientations. Thus, directional growth is not necessarily controlled by the thermal gradient of solidification. We have observed a large number of Si systems that exhibit faceted growth: Si-MoSi₂, Si-Ge-MoSi₂, Si-ZrSi₂, Si-VSi₂ and Si-TaSi₂. Contradictory to Jackson and Hunt model, rod growth has been reported for Si-TiSi₂ [13] and Si-CrSi₂ [24].

3.2. Crucible Selection

The crucible selection was found to be a critical process parameter. All specimens were solidified under identical parameters using BN and SiO₂ crucibles. In order to prevent reaction between SiO₂ crucible and Si/Ge/W melt, 1.5 g of CaCl₂ powder was added to the charge. Liquid CaCl₂ forms a barrier between Si/Ge/W melt and SiO₂ crucible, which eliminated fracturing of the ingot during cooling. Residual CaCl₂ on the ingot surface was removed by rinsing with water [14].

Figure 3 shows the temperature dependent resistivity data for sample 3 ($\text{Si}_{89.8}\text{Ge}_{9.3}\text{W}_{0.9}$) solidified in BN and SiO₂ crucibles. The $\text{Si}_{89.8}\text{Ge}_{9.3}\text{W}_{0.9}$ alloy processed in SiO₂ crucible both had a high resistivity and exhibited a transition from extrinsic to intrinsic semiconductor behavior around 773 K. In conjunction with extrinsic to intrinsic electrical transport behavior, the alloy transitioned from p-type to n-type Seebeck behavior (not shown here). However, the same alloy processed in BN crucible exhibited lower resistivity and extrinsic semiconductor behavior, consistent with greater content of dopants. The Seebeck coefficient was positive for the whole temperature range indicating a dopant controlled electrical behavior.

ICP and nitrogen determination were performed to provide a chemical analysis of the specimens. Figure 4 shows that sample 3 ($\text{Si}_{89.8}\text{Ge}_{9.3}\text{W}_{0.9}$) processed in a BN crucible had significantly higher boron content (0.17 at%) than the specimen derived from the SiO_2 crucible (0.009 at%). The N content was low (≤ 0.04 at%) but it was twice as high for the sample derived from BN crucible. The unexpected presence of boron in the fused silica ingots is likely due to the tendency of boron to reside within the ICP system after measurement. In addition, ICP results of the W raw powder showed 0.0003 at% boron impurity contributing to the unexpected boron content. Boron was not observed in the microstructure as either boron precipitate or within the matrix, possibly due to its low content. XRD also displayed no evidence of second phases formed due to boron contamination or lattice parameter shift. Optimizing the boron content can be beneficial in optimizing the TE properties in the W/Si/Ge system. To emphasize this point a third specimen was prepared by intentional doping of $\text{Si}_{89.8}\text{Ge}_{9.3}\text{W}_{0.9}$ with 1.9 at% B and processed in SiO_2 crucible; whose resistivity was also plotted as a function of temperature in Figure 3. The temperature dependent resistivity behavior of this third ingot was similar to the ingot processed in BN crucible, exhibiting extrinsic semiconductor behavior for the whole temperature range. The absolute values of the resistivity were lower due to the larger content of intentional B-doping. The rest of this paper focuses on specimens processed in BN crucibles. For consistency all BN crucibles were filled to the same levels and subjected to similar solidification profiles. This ensures the contact area, and dopant diffusion kinetics are comparable between samples. Additionally, the thermodynamic solubility limit of B in Si serves to provide a consistent upper limit. Typical RTG samples are doped to the solubility limit, as dopant segregation is a commonly reported phenomenon [30,31]. Since the electrical properties of these samples are similar to RTG properties the doping levels provided by the crucibles is also likely to be near the solubility limit. As a result the sample set is believed to have comparable doping levels, although a controlled doping scheme using fused silica crucibles may be preferable.

3.3. Thermoelectric Properties

Figure 5 shows an Arrhenius plot of electrical conductivity as a function of temperature and composition for all samples processed in BN crucibles, thus B-doped systems as discussed in the previous section (3.2. Crucible Selection). Reported results for p-type $\text{Si}_{80}\text{Ge}_{20}$ are also included in figure 5 for melt derived RTG (zone leveled) [16] and sintered nano-structured materials [25]. The temperature dependent behavior of electrical conductivity was very similar to published results for p-type B doped $\text{Si}_{80}\text{Ge}_{20}$. With increasing temperature the electrical conductivity decreased over the temperature range of 373-1273 K. Composition did not have any effect on the temperature dependent behavior. All the samples exhibited the characteristics of a degenerate semiconductor, metal like σ -T relationship. None of the samples exhibit intrinsic conduction behavior up to 1273 K, the instrumentation limit. Uncertainty was calculated for sample 3 and represents typical measurement uncertainty for all samples. Uncertainty calculations include geometric tolerance of samples/measurement configuration, statistical variation, and multimeter uncertainty. The details of the uncertainty analysis will be published in a future paper. The observed trend in electrical conductivity for the investigated compositions is a uniform reduction in conductivity with increasing Ge concentration (Specimens 1-4 shown with solid symbols, Figure 5) at a given W concentration (0.8 at%). This trend can be understood from the disorder introduced in the matrix as Ge occupies Si lattice sites. Ge on Si sites introduce fluctuations in lattice potential and result in an extra electron scattering term, which is proportional to the fraction of Ge in the alloy [32]. This alloy scattering is non-existent for sample 1, which

contains no Ge, and resulted in the high electrical conductivity of the sample. Samples 2-4 have increasing levels of Ge content and the alloy scattering caused a uniform reduction in electrical conductivity. On average electrical conductivity decreased 68.2% with an increase of Ge content from 0 to 14.9 at% Ge. The samples containing 4.4 and 9.3 at% Ge (samples 2 and 3) exhibit similar electrical conductivity to the published data for both zone-refined and nano-structured p-type $\text{Si}_{80}\text{Ge}_{20}$ [16,25].

Increasing the W content increased the electrical conductivity (Samples 4 and 5) at similar Ge concentrations. Increasing the W at% content from 0.8% to 3% (shown with open symbols, Figure 5) resulted in an enhancement of 79% in the electrical conductivity on average. The work of Nonomura et. al. report tungsten silicide to be a p-type narrow gap semiconductor with an activation energy of 0.005 eV and electrical conductivity of $2.5\text{E}4 \text{ S/m}$ near room temperature [33]. The electrical conductivity of tungsten silicide is lower than all the samples measured in this work. Therefore, the increase in electrical conductivity observed between samples 4 and 5 cannot be explained directly by the presence of the silicide phase. The trend is instead believed to be due to the change in carrier density as a result of the two tungsten levels. Samples 1-3 with 0.8 at% W have carrier densities ranging from $1.2\text{E}20 \text{ cm}^{-3}$ to $2.9\text{E}20 \text{ cm}^{-3}$ while sample 5 with 3 at% W has $8.5\text{E}20 \text{ cm}^{-3}$. As discussed in a previous section (3.1 Microstructure) the tungsten is only found in the precipitates and is not soluble in the matrix. Therefore, the carrier density difference may be a result of the silicide phase influencing the solubility limit of boron in the $\text{Si}_x\text{Ge}_{1-x}$ matrix. The effect of Ge content on the electrical properties was independent of the W content, thus further increase in Ge content up to 25% for compositions with 3 at% W resulted in a decrease in conductivity; even though the absolute values are still higher than the compositions with smaller amount of W. For example, even the composition with 25 at% Ge had same conductivity, for the whole temperature range, as the composition with 0 at% Ge, when the W content is increased from 0.8 at% to 3 at%.

The temperature dependence of Seebeck coefficient for the same set of samples is shown in Figure 6. All samples exhibited p-type behavior over the temperature range investigated. The measured values fell in the range of 70 to 300 $\mu\text{V/K}$. Seebeck coefficient increased with temperature; typical behavior for a degenerate extrinsic semiconductor. Uncertainty was calculated for sample 3 and represents typical uncertainties of all samples. The uncertainty accounts for the probe wire Seebeck uncertainty, statistical variation, multimeter uncertainty, and the cold finger effect. The cold finger effect is an artifact of the four point measurement configuration, in which heat is parasitically transferred down the probe length. The effect leads to an over-estimation of the Seebeck coefficient. The total uncertainty was estimated with a thermal FEA along with standard measurement error propagation, the details of which will be addressed in a future publication. The 0.8 at% W samples (shown with solid symbols, Figure 6) all exhibit Seebeck coefficients higher than published values for p-type $\text{Si}_{80}\text{Ge}_{20}$ [16,25]. At low temperature the Seebeck coefficients decrease slightly with increasing Ge content, up to sample 4 with 14.9 at% Ge. The high Seebeck coefficient combined with comparable electrical conductivity leads to power factor improvements as large as 50% over RTG. Seebeck enhancement of PbTe has been discussed by Faleev and Leonard [34] by introducing metallic precipitates into a PbTe matrix. Band bending at the interface can filter low energy electrons and leave high energy electrons undisturbed, leading to enhanced Seebeck coefficient and power factor for the composite. The observed trend is explained by the electron filtering phenomenon, although the phenomenon is dependent on precipitate size and can therefore not explain the trend observed in this micron-scale system. At this time the enhancement of power factor is not clearly

understood. The 3 at% W samples (shown with open symbols, Figure 6) have lower Seebeck coefficients than the 0.8 at% samples. The decrease is consistent with carrier concentration data, which is higher for the 3 at% W samples.

Figure 7 shows the total thermal conductivity of the compositions investigated and the lattice thermal contribution calculated by the Wiedemann-Franz law. Uncertainty on total thermal conductivity is estimated to be 5% [35] and the lattice uncertainty considers uncertainty on both electrical and thermal conductivity. Addition of Ge to the matrix initially reduced the thermal conductivity significantly over the entire temperature range of interest; the inset shows the rescaled thermal conductivity plot to show the results for the composition with no Ge (Figure 7A). After the initial large reduction in thermal conductivity smaller reductions were obtained with additional Ge, samples 2-4. However, there was no observable trend as the Ge content increased to greater values. A least squares regression was used to interpolate thermal conductivity data in order to calculate the lattice thermal contribution and ZT. The correlation coefficient of the thermal data ranges from 0.76 to 0.98, the statistical uncertainty of the measurement data is understood to provide the low correlation, but the regression is still thought to provide accurate averages for the purpose of calculating figure of merit and lattice contribution. A more complicated fitting method would model the statistical variation of the measurement rather than focusing on capturing the representative values. The Wiedemann-Franz law estimates the lattice contribution of thermal conductivity as follows:

$$\lambda_{Lat} = \lambda_{Total} - L\sigma T \quad (2)$$

$$L = \frac{\pi^2 k_b^2}{3e^2} \quad (3)$$

Where λ_{Lat} is the lattice thermal contribution, λ_{Total} the total thermal conductivity, T the temperature, σ the electrical conductivity, and L Lorenz number. The Lorenz number is classically approximated from k_b the Boltzmann constant and the charge of an electron e.

Lattice thermal conductivity decreased significantly with the initial increase in Ge content (specimens 1 and 2, Figure 7B inset). As the Ge content increased further samples 2 to 4, smaller reductions in the lattice thermal conductivity was observed, with values almost unchanged between specimens 3 and 4 for the whole temperature range. The trend is understood as a result of phonon scattering by the mass difference of Si and Ge [20,26,28,36]. Increasing the W content sample 4 to 5 resulted in a minor decrease in lattice thermal conductivity; as the total thermal conductivity remained similar despite increasing electrical conductivity. The alloy composition with the lowest lattice thermal conductivity was specimen 5 with values similar to the lattice thermal conductivity of published data for p-type RTG $\text{Si}_{80}\text{Ge}_{20}$ [16]. The higher lattice thermal conductivities of the samples, as compared to RTG, are due to a combination of the lower Ge content and the observed micro-segregation of the samples (Figure 1). The work of Lee and Hwang [37] theoretically demonstrate the importance of homogeneous segregation of the Si/Ge matrix. In the simulations of Lee and Hwang clusters of Ge atoms are found to significantly increase the thermal conductivity, as clusters of Ge atoms reduce the number of Si-Ge bonds which provide the desired phonon scattering. Increases as large as 3x are calculated for Ge precipitates of 2nm [37]. The trend in samples 5-7 is counter intuitive as conductivity increases with increasing Ge content. The behavior may be a result of increased micro-segregation of the Ge as a result of the higher 3 at% W phase. In the previous section (3.1 Microstructure) Ge

segregation was observed to be correlated with the silicide precipitates. The higher W content may be driving more Ge micro-segregation, leading to increased conductivity.

Table 2: Calculated thermal conductivity of composite samples

Sample #	Si at% in Matrix	Silicide V.F. %	Thermal Conductivity (W/m-K) at 300K			
			Matrix [26]	Precipitate [27]	Composite Calculated	Measured
1	100.0	1.7	59.6	46.6	59.3	60
2	95.6	1.8	14	46.6	14.2	12
3	90.5	1.9	8.8	46.6	8.96	8
4	84.8	1.7	6.8	46.6	6.91	6
5	84.0	6.5	6.8	46.6	7.26	7
6	78.7	6.4	4.8	46.6	5.15	8
7	73.4	6.4	4.4	46.6	4.72	14

The 10-100 μ m scale of precipitates and low volume fraction of the composites allows for a straight-forward estimation of the thermal conductivity. The precipitate/matrix interface surface area, normalized with bulk volume, is estimated to be 10 cm²/cm³ for the samples in this study. To provide a contrast, the surface area per volume of a nano-structured composite containing 10nm precipitates has on the order of 1E5 cm²/cm³. The surface area is calculated assuming spherical precipitates and employing the range of volume fractions for the samples in this work. The influence of phonon scattering at the interface of the silicide precipitates should be negligible for the samples of this work. Therefore a straight-forward estimation of thermal conductivity can be based on considering the samples as composite bodies of two phases, the Si_xGe_{1-x} matrix and tungsten silicide precipitates. As previously discussed the thermal conductivity of the matrix will be strongly dependant on the alloying level of Si_xGe_{1-x} [26,28,20,36]. Additionally, the dopant level will have a large influence on thermal conductivity as point scattering inhibits phonon transport. To gain a deeper understanding, without unneeded complexity, the matrix of the samples is assumed to be homogeneous, i.e. no micro-segregation of Si_xGe_{1-x}, with doping levels comparable between samples. The precipitates are modeled as a periodic arrangement of tungsten silicide cubes with side length 50 μ m. Figure 8 shows the simplified model of the composite, with the repeating unit highlighted. The geometry of the repeating unit (captured by x and the precipitate size d) is a function of the area fraction (γ) of the precipitate phase, which can be estimated from the nominal volume fraction of the silicide phase.

$$x = \frac{d(\sqrt{4+\gamma}-3\sqrt{\gamma})}{2\sqrt{\gamma}} \quad (4)$$

$$\lambda_{Composite} = \frac{(2d+x)}{(d+x)} \left[\frac{x \cdot \lambda_{Matrix}}{(2d+x)} + \frac{1}{\frac{(d+x)}{d \cdot \lambda_{Matrix}} + \frac{1}{\lambda_{Precipitate}}} \right] \quad (5)$$

The composite thermal conductivity can be estimated by considering the series/parallel nature of the components of the repeating unit. The method employed is classically used for the analysis of composite bodies under steady thermal conduction [29]. Table 2 shows the predicted influence of the silicide phase on the samples. The silicon at% used for the calculations are the nominal level of silicon minus the silicon consumed by the silicide phase. These levels compare well to average values measured with EDS and ICP (3.1 Microstructure). The matrix thermal

conductivity is calculated based on the experimental work of Maycock [26]. The silicide volume fraction is used to establish the geometry of the model. For sample 1 the calculated composite conductivity is lower than the matrix conductivity, as a result of the relatively lower conductivity of the precipitate phase. For the remaining samples 2-7 the calculated composite conductivity are higher than the matrix conductivity as a result of the precipitates. The precipitate driven increase in thermal conductivity is undesirable for these samples, but the calculation shows an average increase of 1.6% for the 0.8 at% W samples and 7.1% for the 3 at% W samples. Compared to the 50% improvement of electrical properties the silicide precipitates are found to be desirable.

The figure of merit is shown in Figure 9. Similar to $\text{Si}_{80}\text{Ge}_{20}$ alloy, the ZT increases in value over the measured temperature range. Trends in Seebeck coefficient as a function of composition dominated the trends in the calculated ZT values for a given W content. ZT maximized for the specimen 3 for the whole temperature range. At higher Ge contents (samples 5-7) the ZT did not change in any significant amount similar to the observations in Seebeck coefficient. However, electrical conductivity was the dominant factor in deciding the trends in ZT as a function of W content; thus the ZT increased slightly with increasing W content, samples 4 to 5, despite a decrease in Seebeck coefficient. This was due to the greater increase in electrical conductivity even though the ZT changes with square of Seebeck coefficient. The optimal composition from this investigation with a ZT near RTG was found to be 0.8 at% W/9.3 at% Ge (Sample 3). This sample was created without the need for lengthy zone leveling. The results suggest that W addition can reduce the use of expensive Ge component of the alloy.

4. Conclusion

The work presented has demonstrated the feasibility of a W/Si/Ge system for high temperature thermoelectric applications. Directional solidification in the W/Si/Ge system resulted in formation of randomly ordered WSi_2 precipitates and micro-segregation of Ge. Large WSi_2 precipitates are observed, exhibiting faceted growth. Processing in BN crucibles resulted in B dissolution in the melt on the order of 0.17 at%. The ability to control the dopant level through the use of more readily available fused silica crucibles provides another parameter for optimizing the system.

W addition with B doping enhances electrical properties. Seebeck coefficients on the order of $+300 \mu\text{V/K}$ along with electrical conductivities around $2.8 \times 10^4 \text{ S/m}$ and high power factors up to $3,000 \mu\text{W/m-K}^2$ was observed over the temperature range of 373-1173 K. The highest power factor was achieved at a composition of $\text{Si}_{89.8}\text{Ge}_{9.3}\text{W}_{0.9}$; power factor is 50% higher than published results for sintered and zone-leveled $\text{Si}_{80}\text{Ge}_{20}$. Strong electrical properties combined with good thermal conductivity resulted in a figure of merit comparable to the traditional high temperature $\text{Si}_x\text{Ge}_{1-x}$ materials developed by NASA for use in RTGs.

References

1. W. P. Lange & R.G. Carroll, Review of recent advances of radioisotope power systems, *Energy Conversion Management* 49 (2008) 393.
2. J. M. O. Zide et al., High efficiency semimetal/semiconductor nanocomposite thermoelectric Materials, *J. App. Phy.* 108 (2010) 123702.

3. Elliott, R., *Eutectic Solidification Processing*, Butterworths & Co., London, (1983).
4. A.M. Dehkordi & D. Vashaee, Enhancement in thermoelectric power factor of polycrystalline $\text{Bi}_{0.5}\text{Sb}_{1.5}\text{Te}_3$ by crystallite alignment, *Physica Status Solidi (a)* 209 (2012) 2131.
5. T. Ikeda et al., Self-Assembled Nanometer Lamellae of Thermoelectric PbTe and Sb_2Te_3 with Epitaxy-like Interfaces, *Chem. Mater.* 19 (2007) 763.
6. J. R. Sootsman et al., Microstructure and Thermoelectric Properties of Mechanically Robust PbTe-Si Eutectic Composites, *Chem. Mater.* 22 (2010) 869.
7. J. Androulakis et al., Spinodal Decomposition and Nucleation and Growth as a Means to Bulk Nanostructured Thermoelectrics: Enhanced Performance in $\text{Pb}_{1-x}\text{Sn}_x\text{Te-PbS}$, *J. Am. Chem. Soc.* 129 (2007) 9780.
8. E. Quarez et al., Nanostructuring, compositional fluctuations, and atomic ordering in the thermoelectric materials $\text{AgPb}_m\text{SbTe}_{2+m}$: The myth of solid solutions, *J. Am. Chem. Soc.* 127 (2005) 9177.
9. H. Wu et al., Ternary eutectic growth of nanostructured thermoelectric Ag-Pb-Te materials, *Appl. Phys. Lett.* 101 (2012) 23107.
10. C.B. Vining, "Thermoelectric Properties of Silicides" 277, *CRC Handbook of Thermoelectrics*, Ed. D.M. Rowe, CRC Press, London, (1995).
11. S. K. Bux et al., Mechanochemical synthesis and thermoelectric properties of high quality magnesium silicide, *J. Mat. Chem.* 21 (2011) 12259.
12. N. Mingo et al., Nanoparticle-in-alloy approach to efficient thermoelectrics: Silicides in SiGe , *Nano Lett.* 9 (2009) 711.
13. F.W. Dynys & A. Sayir, Self assemble silicide architectures by directional solidification, *J. Eur. Ceram. Soc.* 25 (2005) 1293.
14. P. Ravishankar, Liquid Encapsulated Bridgman (LEB) method for directional solidification of silicon using calcium chloride, *J. Crystal Growth* 94 (1989) 62.
15. L.M. Clark & R.E. Taylor, Radiation loss in the flash method for thermal diffusivity, *J. App. Phys.* 2 (1975) 714-719.
16. Silicon Germanium Thermoelectric Materials and Module Development Program (U), RCA Topical Report, Contract AT(29-2)-2510, (1969).
17. PDF 01-072-6182 (ICDD, 2008).
18. PDF 04-006-2527 (ICDD, 2005).
19. A. Leineweber & E. J. Mittemeijer, Anisotropic microstrain broadening due to compositional inhomogeneities and its parametrisation, *Z. Kristallog. Suppl.* 23 (2006) 117.
20. J. P. Dismukes et al., Thermal and Electrical Properties of Heavily Doped Ge-Si Alloys up to 1300°K , *J. App. Phys.* 35 (1964) 2899.

21. K.A. Jackson & J.D. Hunt, Lamellar and Rod Eutectic Growth, *Trans. Metall. Soc. AIME* 236 (1966) 1128.
22. B. Vinet et al., Correlations between Surface and Interface Energies with Respect to Crystal Nucleation, *J. Colloid Interface Sci.* 255 (2002) 363.
23. S.V. Meschel & O.J. Kleppa, Standard enthalpies of formation of some 3d transition metal silicides by high temperature direct synthesis calorimetry, *J. Alloys Compd.* 267 (1998) 128.
24. L.M. Levinson, Highly anisotropic columnar structures in silicon, *Appl. Phys. Lett.* 21 (1972) 15.
25. G. Joshi et al., Enhanced Thermoelectric Figure-of-Merit in Nanostructured p-type Silicon Germanium Bulk Alloys, *Nano Letters* 8 (2008) 12.
26. P.D. Maycock, Thermal conductivity of silicon, germanium, III-V compounds and III-V alloys, *Solid-State Electronics*, **10** (1967) 161-168.
27. V.S. Neshpor, The thermal conductivity of the silicides of transition metals, *J. Eng. Phys. Thermophys.* **15** (1968) 321-325.
28. B. Abeles, D. Beers, G. Cody, J.P. Dismukes, Thermal conductivity of Ge-Si alloys at high temperatures, *Phys. Rev.* **125** (1962) 44-46.
29. V. Arpaci, *Conduction Heat Transfer* (Addison-Wesley Pub. Co., 1966).
30. D.M. Rowe, N. Savvides, The reversal of precipitation in heavily doped silicon-germanium alloys, *J. Phys. D.* **12** (1979) 1613-1619.
31. Z. Zamanipour, J.S. Krasinski, D. Vashaee, Comparison of boron precipitation in p-type bulk nanostructured and polycrystalline silicon germanium alloy, *J. Appl. Phys.* **113** (2013) 143715.
32. G.A. Slack, M.A. Hussain, The maximum possible conversion efficiency of silicon-germanium thermoelectric generators, *J. Appl. Phys.* **70** (1991) 2694-2718.
33. T. Nonomura et. al., Thermoelectric properties of group VI metal silicide semiconductors, *Physics Procedia* **11** (2011) 110-113.
34. S.V. Faleev, F. Leonard, Theory of enhancement of thermoelectric properties of materials with nanoinclusions, *Phys. Rev. B* **77** (2008) 214304.
35. W. Parker, R. Jenkins, C.P. Butler, G.L. Abbott, Flash method of determining thermal diffusivity, heat capacity, and thermal conductivity, *J. Appl. Phys* **32** (1961) 1679-1684.
36. B. Abeles, Lattice thermal conductivity of disordered semiconductor alloys at high temperatures, *Phys. Rev.* **131** (1963) 1906-1911.
37. Y. Lee, G.S. Hwang, Microsegregation effects on the thermal conductivity of silicon-germanium alloys, *J. Appl. Phys.* **114** (2013) 174910.

38. Z. Zamanipour, D. Vashaee, Comparison of properties of p-type nanostructured bulk $\text{Si}_{0.8}\text{Ge}_{0.2}$ alloy with $\text{Si}_{0.8}\text{Ge}_{0.2}$ composites embedded with CrSi_2 nano-inclusions, J. Appl. Phys. **112** (2012) 093714.
39. Y. Ezzahri, K. Joulain, Effect of embedding nanoparticles on the lattice thermal conductivity of bulk semiconductor crystals, J. Appl. Phys. **113** (2013) 043510.

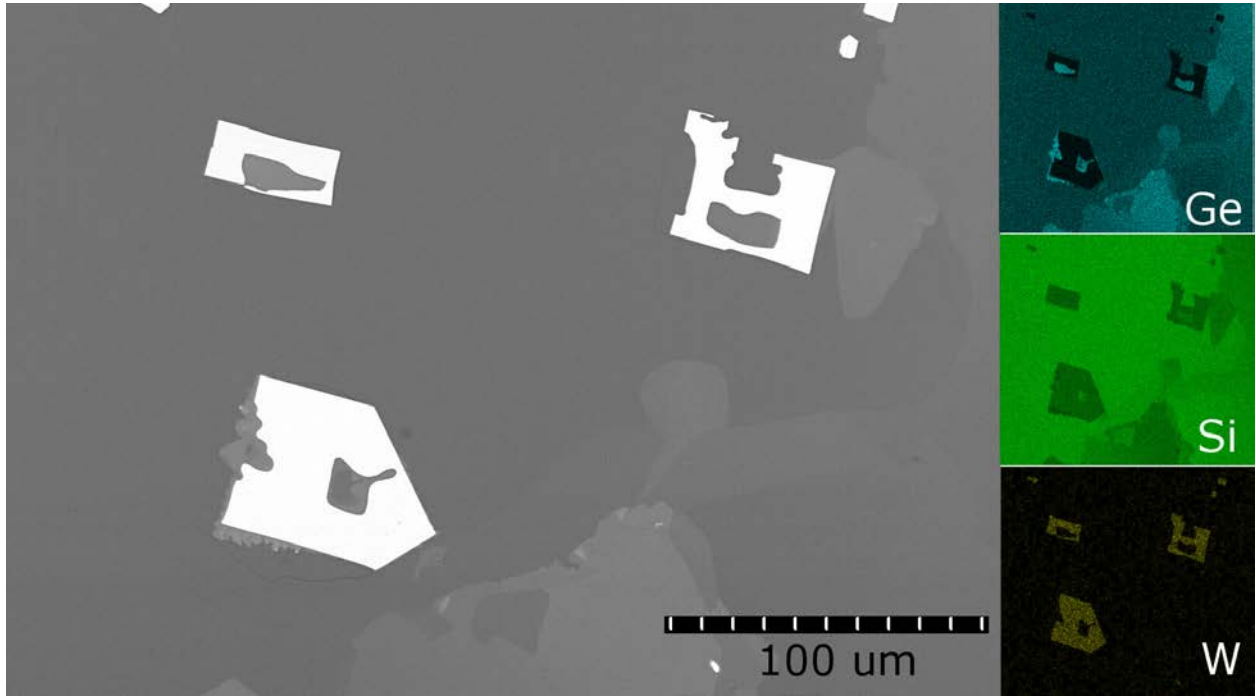


Figure 1: Back-scattered SEM image (left) with EDS chemical maps (right) of Ge, Si, and W. Large WSi_2 precipitates (white faceted precipitates) can be observed in an inhomogeneous Si/Ge matrix.

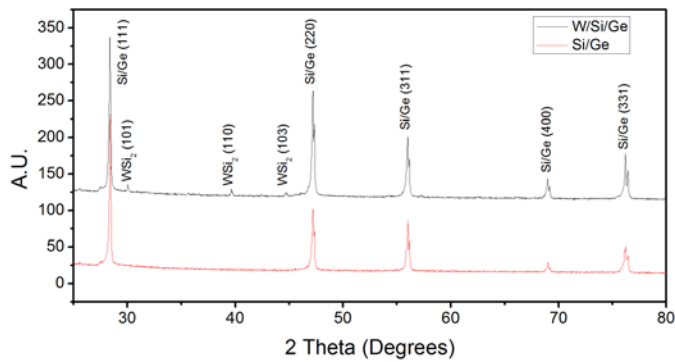


Figure 2: XRD Pattern for Sample 3, $\text{Si}_{89.8}\text{Ge}_{9.3}\text{W}_{0.9}$ (top), and $\text{Si}_{90}\text{Ge}_{10}$ (bottom), addition of W forms WSi_2 second phase with no shift in Si/Ge reflections.

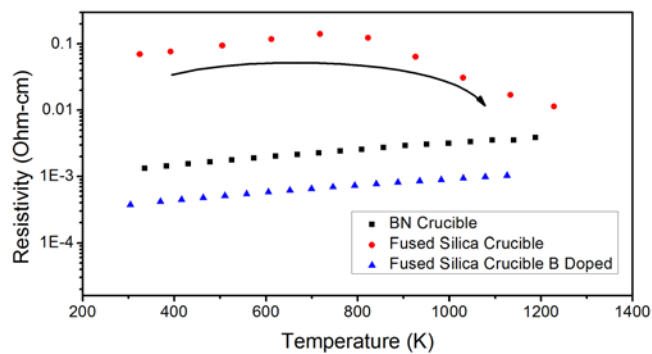


Figure 3: Electrical resistivity of three comparable samples prepared using BN or SiO₂ crucibles. Trend indicates un-intentional doping resulting from the BN crucible.

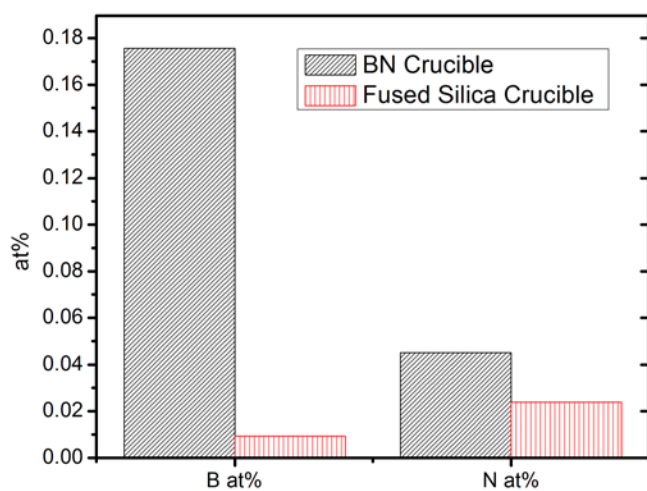


Figure 4: Composition for ingots prepared in BN and SiO₂ crucibles as determined by ICP and Nitrogen determination. Samples are not intentionally doped.

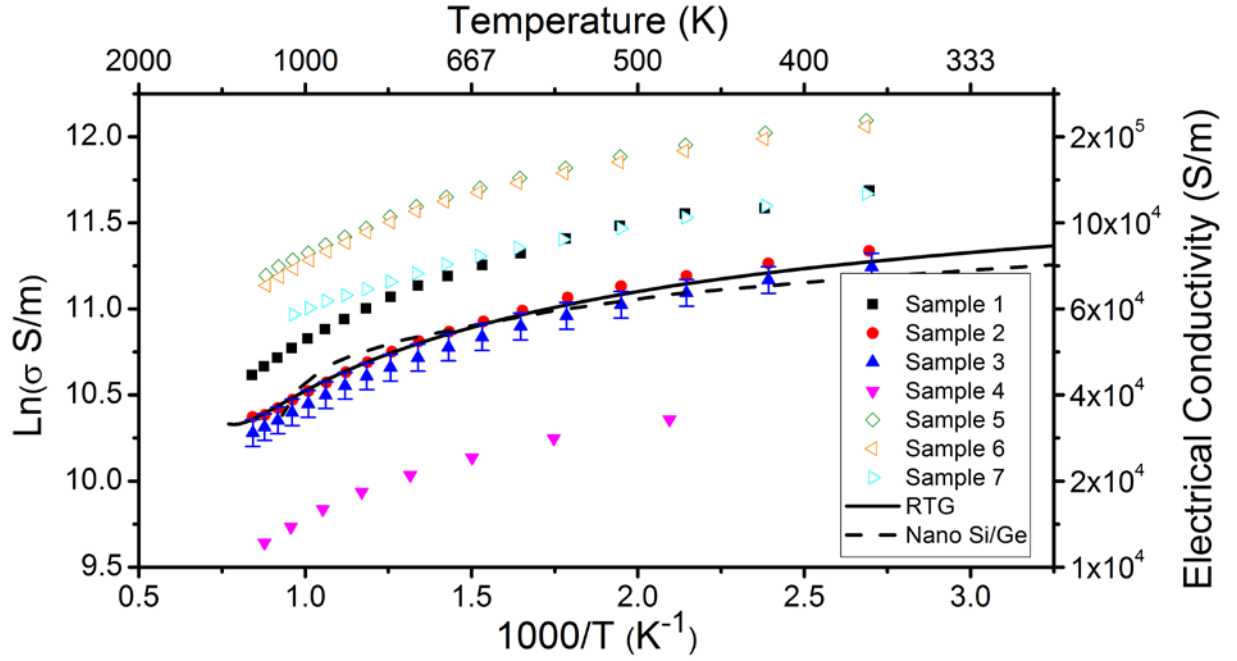


Figure 5: Arrhenius plot of electrical conductivity of several W/Si/Ge samples. Closed symbols represent 0.8 at% W, open symbols 3 at% W. Included are published values for RTG [16] and nano-structured [25] $\text{Si}_{80}\text{Ge}_{20}$ alloys.

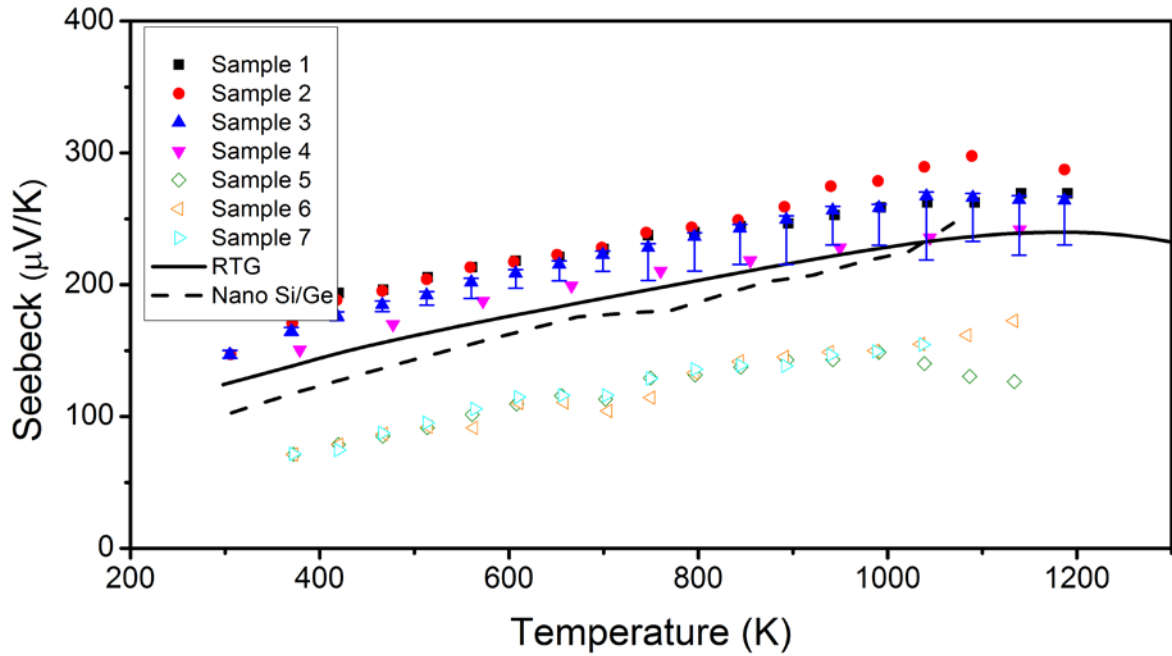


Figure 6: Seebeck coefficient of several W/Si/Ge samples. Closed symbols represent 0.8 at% W, open symbols 3 at% W. Included are published values for RTG [16] and nano-structured [25] $\text{Si}_{80}\text{Ge}_{20}$ alloys.

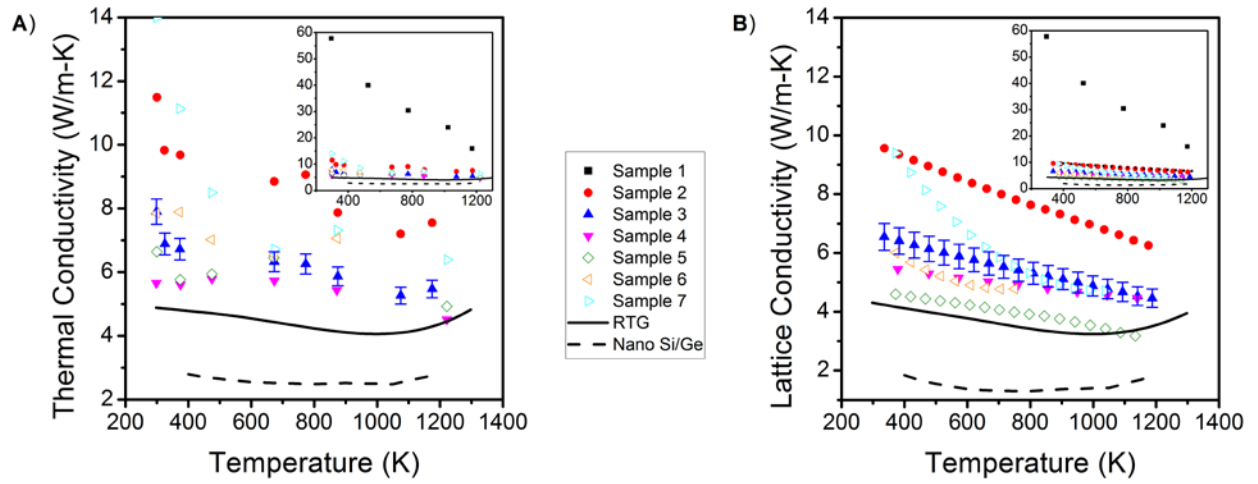


Figure 7: A) Total thermal conductivity of several W/Si/Ge samples. B) Calculated lattice thermal conductivity component. Closed symbols represent 0.8 at% W, open symbols 3 at% W. Included are published values for RTG [16] and nano-structured [25] $\text{Si}_{80}\text{Ge}_{20}$ alloys.

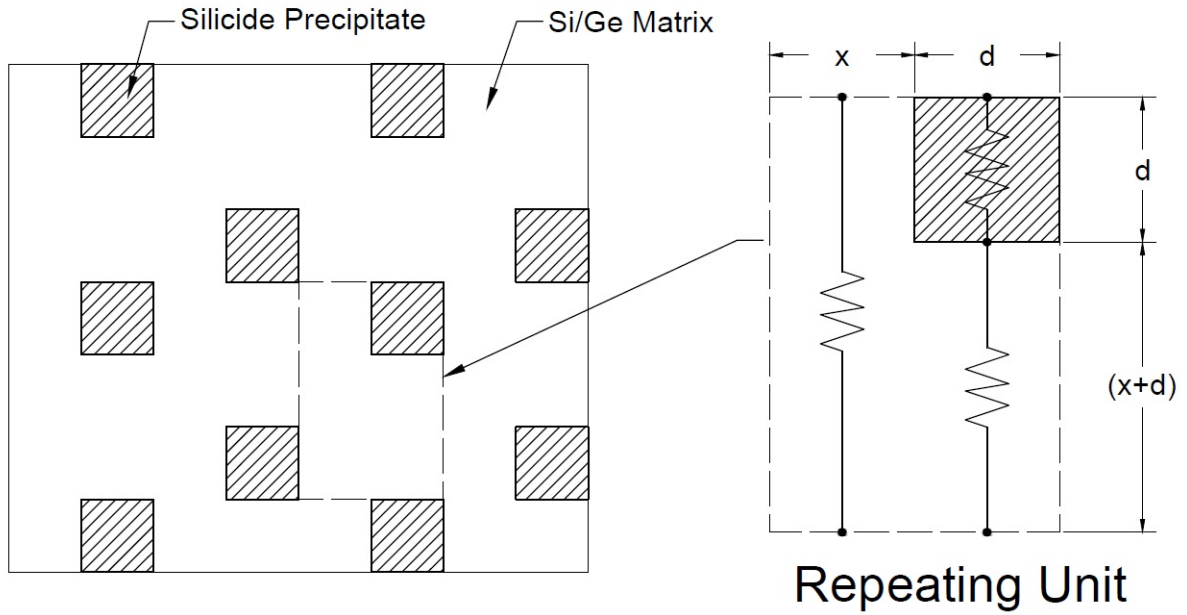


Figure 8: Schematic diagram of Si/Ge matrix with silicide precipitate. Repeating unit highlighted to the right to outline the geometric parameters x and d .

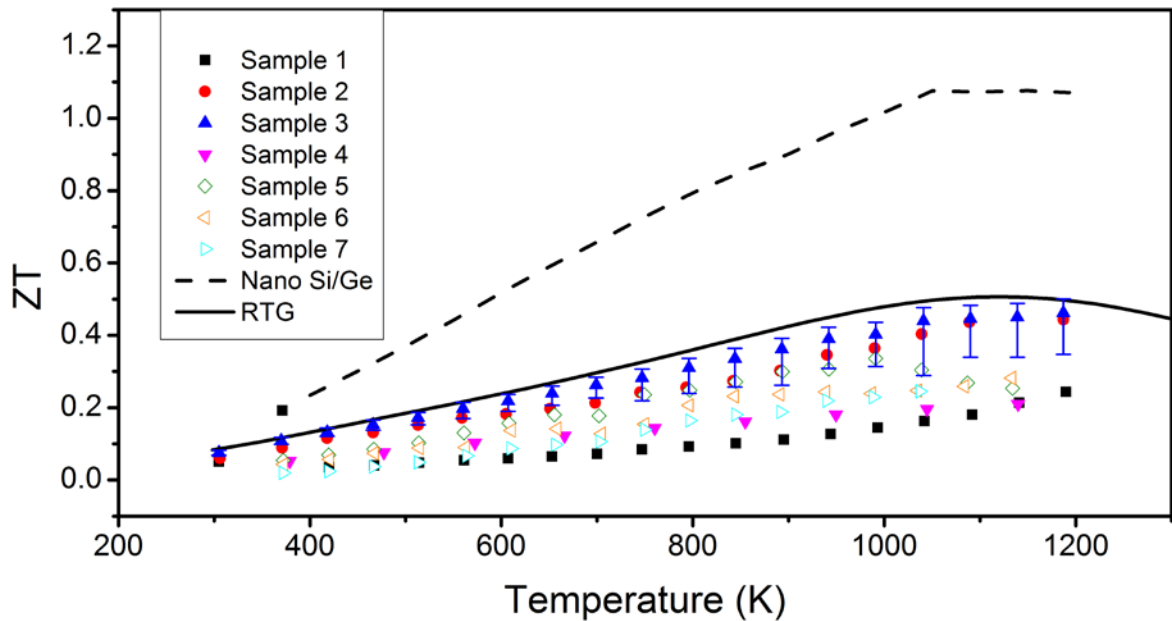


Figure 9: Figure of Merit (ZT) of several W/Si/Ge samples. Closed symbols represent 0.8 at% W, open symbols 3 at% W. Included are published values for RTG [16] and nano-structured [25] $\text{Si}_{80}\text{Ge}_{20}$ alloys.

Effect of Zr substitution by Ti on growth direction and interface structure of $\text{LaB}_6 - \text{Ti}_x\text{Zr}_{1-x}\text{B}_2$ directionally solidified eutectics¹

In collaboration with I. Jouanny^a, M. Sennour^a, M.H. Berger^{a2}, V.B. Filipov^b, A. Ievdokymova^b, V.N. Paderno^b, A. Sayir^c

^a MINES-ParisTech, Centre des Matériaux, UMR CNRS 7633, 91003 Evry Cedex, France

^b Frantsevitch Institute for Problems of Materials Sciences, Nal. Ac. of Sci of Ukraine, Kiev, Ukraine

^c Case Western Reserve University, Cleveland OH 44135, USA

Boride ceramics were directionally solidified around $\text{LaB}_6 - (\text{Ti}_x\text{Zr}_{1-x})\text{B}_2$ eutectic compositions. The directionally solidified rods were composed of LaB_6 rich concentric belts surrounding large eutectic regions with a dense and uniform distribution of $(\text{Ti}_x\text{Zr}_{1-x})\text{B}_2$ fibers of 0.6 μm in diameter inside a LaB_6 matrix. The mole fractions of diboride at the hexaboride-diboride eutectic points have been more accurately defined for the range of composition $x = 0$ to 0.76. Fiber growth directions were modified by the addition of titanium. Diboride (subscript 2) fibers grew along $[0001]_2$ for $x = 0$ and along $\langle \bar{1}100 \rangle_2$ for $x \neq 0$. These axes were tilted in regard to rod axes, of about 25 to 30° for $x = 0$ and 8 to 15° for $x \neq 0$. The orientation of the hexaboride

(subscript 6) matrix was unchanged with or without titanium addition and the $\langle 210 \rangle_6$ direction was close to the rod axis. Due to a strong anisotropy of CTEs in the diborides, the change in fiber growth axis should modify the stress levels in the fibers, switching from tensile ones for $x = 0$ to compressive ones for $x \neq 0$. The favored crystallographic orientation relationship between matrix and fibers was described as follows: $[001]_6//[0001]_2$ and $(110)_6//(11\bar{2}0)_2$ and $(\bar{1}10)_6//(\bar{1}100)_2$ for any x value. Fibers tended to develop faceted interfaces, the dominant ones were $\{110\}_6//\{11\bar{2}0\}_2$ for $x=0$ and $(001)_6//(0001)_2$ for $x \neq 0$, the latter being expected to be energetically more favorable, as predicted by a 2D geometrical model. These changes in fiber growth direction and facet types are expected to improve the mechanical properties and failure mechanisms of the material.

1. Introduction

Lanthanum hexaboride (LaB_6) single-crystal ceramics are used as hollow cathode materials in electric propulsion systems [1] due to good emissive properties, high thermo-ionic current densities, a thermomechanical stability under ion bombardment at elevated temperatures and the possibility of reactivation after poisoning. However, LaB_6 single crystals have a brittle behavior and a low thermal shock resistance [2] which represents a strong drawback when manufacturing LaB_6 items of complex shapes and for their long term use. To address this challenge, LaB_6 - MeB_2 in-situ composites were developed, by directional solidification of the corresponding eutectics, where Me represents a transition metal such as Ti, Zr, Hf or V. A cooperative growth, from a melt at the eutectic invariant point, results in a LaB_6 ceramic matrix embedding MeB_2 fibers [3-6]. This class of Directionally Solidified Eutectics (DSEs) is known to display a highly organized microstructure with a uniform distribution of fibers showing specific orientation relationships with the matrix. The mechanical properties of DSE composites, such as the bend strength and the fracture toughness [3,7], are improved with regard to LaB_6 single-crystal due to crack deflection at the fiber/matrix interface, fiber bridging and fiber pull out [3,5,7-9]. Moreover, the emissive properties of DSE composites are also improved [7]. The electron emission density is higher for LaB_6 - MeB_2 composites (Me: Zr, Ti, Hf) than for LaB_6 and the maximum density is obtained at the eutectic composition. Thus, LaB_6 - ZrB_2 DSE composite is one of the best candidates for the electrode application in space propulsion due to its good mechanical properties and electron emission performances [3, 7].

LaB_6 has a CaB_6 -type primitive cubic structure ($a = 0.4157$ nm), in which boron octahedra are located at the center of a La cube [10]. ZrB_2 has an AlB_2 -type hexagonal structure ($a = 0.3169$ nm, $c = 0.3530$ nm) which is highly anisotropic. Graphite-like sheets of boron alternate perpendicular to the c -axis, with closed packed metal layers [11]. The favored crystallographic orientation relationship between LaB_6 hexaboride (subscript 6) and ZrB_2 diboride (subscript 2) is described by $[001]_6//[0001]_2$ and $\{110\}_6//\{11\bar{2}0\}_2$ [7,12,13]. It is assumed that the two structures share part of the boron atoms at the $\text{LaB}_6/\text{ZrB}_2$ interfaces. The misfit between boron-boron bond lengths in LaB_6 and ZrB_2 structures ($\text{B-B} = 0.1766$ nm for LaB_6 and 0.1829 nm for ZrB_2) could be reduced by substituting some zirconium by titanium atoms of lower atomic radii ($\text{B-B} = 0.1750$ nm in TiB_2) [14]. The occurrence of a $(\text{Ti}_x\text{Zr}_{1-x})\text{B}_2$ solid solution enables modification of the B-B length in the diboride phase toward that in LaB_6 [15]. A series of DSE rods with various x values has been synthesized to determine the influence of titanium insertion in ZrB_2 on the structure and mechanical behavior of the diboride/hexaboride interfaces. This

article focuses on the investigation of the growth direction, crystallographic relationship and aims to elucidate the structure of interfaces for the $\text{LaB}_6\text{-(Ti}_x\text{Zr}_{1-x})\text{B}_2$ eutectic ceramics for wide range of compositions, $0 \leq x \leq 0.76$.

2. Experimental Procedure

Six $\text{LaB}_6\text{-(Ti}_x\text{Zr}_{1-x})\text{B}_2$ composites, $x=0$ to $x=0.76$, were produced by directional solidification using the Bridgman technique [3].

Iodide refined titanium, iodide refined zirconium (99.99% pure), lanthanum oxide (99.997% pure) and amorphous boron (99.9% pure) were used for the synthesis of respective boride starting powders. Titanium diboride and zirconium diboride syntheses were accomplished by self-propagating high-temperature synthesis, while lanthanum hexaboride was synthesized by borothermal reduction. The synthesized materials were subsequently crushed into powders. These powders were mixed in the required proportion, compacted by cold pressing and then sintered at 1700°C in vacuum. Table 1 summarizes the nominal composition of the starting materials used in this study. The molar fraction of diboride phase at eutectic composition, denoted y , is indicated as a function of titanium cationic ratio.

Directional crystallization has been carried out in a high-frequency crucible-free zone melting apparatus "Kristal-111" (working frequency: 0.88 MHz). In order to exclude any possible influence of crystallographic orientation on crystallization conditions and properties of in-situ formed composites, the same LaB_6 single crystal has been used as seed material for all grown samples. Moreover, identical processing conditions were maintained for all samples, i.e., gas overpressure in the working chamber, feed rate of the green body during synthesis, crystallization rate, and mixing (rotation) conditions.

Chemical analyses of $\text{LaB}_6\text{-y(Ti}_x\text{Zr}_{1-x})\text{B}_2$ composites were carried out on cross sections by Wavelength-Dispersive X-ray Spectroscopy (WDX) using a Cameca SX100 electron microprobe. Chemical analyses on single fibers could not be performed by WDX due to the size of fibers (about $0.6\text{ }\mu\text{m}$ in diameter) with respect to the volume of the electron interaction zone. Therefore it was decided to favor elemental resolution rather than spatial resolution and to determine the eutectic composition from a zone including around 100 fibers. A defocused electron probe of $20\text{ }\mu\text{m}$ in diameter was used at 15 kV and 40 nA. The analysis depth was estimated at $1\text{ }\mu\text{m}$. The chemical composition of $\text{LaB}_6\text{-y(Ti}_x\text{Zr}_{1-x})\text{B}_2$ eutectics were determined from an average of ten measurements.

Local variations of the composition were studied by Energy-Dispersive X-ray (EDX) Spectroscopy using a FEI Tecnai F20-ST transmission electron microscope in scanning mode (STEM) and equipped with an EDAX detector. Compositional profiles were performed across a single fiber using a probe size of about 2 nm in diameter. The variation of boron concentration was not measured because these standardless semi-quantitative EDX analyses were not accurate enough to quantify light elements.

The lattice parameters of $(\text{Ti}_x\text{Zr}_{1-x})\text{B}_2$ diborides were determined by X-ray Diffraction (XRD) in Bragg-Brentano geometry (Siemens D500 diffractometer in $(\theta, 2\theta)$ mode, $\text{Cu K}\alpha$ radiation). A 360° continuous rotation around the rod axis was imposed for each detector position. Crystal

orientations of LaB_6 and $(\text{Ti}_x\text{Zr}_{1-x})\text{B}_2$ in the rods were determined using X-ray pole figures performed using a CGR goniometer and a beam width of $2 \times 2 \text{ mm}^2$. The cross-sections were fixed on a Dosophatex sample support, allowing rotations around two orthogonal axes: the normal of the disk (azimuthal angle ϕ from 0 to 360° , with a 3.6° step) and a tilt axis parallel to the surface of the disk (tilt angle χ from 0 to 36° , with a 3.6° step). The X-ray detector was fixed at four successive positions to record diffraction from 2 set of planes for each phase.

The crystal orientation relationships between LaB_6 and $\text{Ti}_x\text{Zr}_{1-x}\text{B}_2$ and interface structure were studied on cross-sections by Selected Area Electron Diffraction (SAED) and High-Resolution Transmission Electron Microscopy (HRTEM) using a Tecnai F20-ST. Thin-foils were extracted from the central parts of the rods, where the uniform distribution and shape of the fibers is characteristic of a cooperative eutectic growth. Parallelepipeds of $2 \times 2 \text{ mm}^2$ square and around 1 mm thick were cut and mechanically thinned down to 10-15 μm . A Gatan® PIPS ion mill was used for a final thinning down to electron transparency. The orientation relationships between fibers and matrix were studied from SAED patterns recorded in the matrix and fiber both at the vicinity of the fiber/matrix interface. Zone axes of low indices were selected with a double-tilt specimen holder and Kikuchi lines were used to obtain a better accuracy on the values of α and β tilt angles. Finally, the stereographic projections of fibers and adjacent matrix were established from these α , β values. The study of interface structure was carried out by HRTEM.

3. Results

3.1 Chemical and structural characterization

Optical micrographs of $\text{LaB}_6\text{-y}(\text{Ti}_x\text{Zr}_{1-x})\text{B}_2$ cross sections displayed the typical morphology of boride eutectics obtained by directional solidification. Concentric lanthanum-rich belts separate regions with a dense and uniform distribution of diboride fibers inside the LaB_6 matrix as described by Deng et al. [8] on $\text{LaB}_6\text{-ZrB}_2$ eutectic rods. The mean radius of fibers was about 0.6 μm (Figure 1a) and did not vary with the TiB_2 phase fraction. At the edge of the belts and close to rim regions irregular growth of the diboride phase was observed. Regions of dense and regular distribution of fibers resulted from a stationary cooperative growth at the eutectic invariant point. The presence of LaB_6 rich belts indicated that the global composition of the solidified rod was shifted from the eutectic point to a hypoeutectic composition.

The average chemical compositions of regions with dense regular packing of diboride fibers were determined by WDX to assess the composition at the eutectic points more precisely. Table 2 lists the chemical compositions of $\text{LaB}_6\text{-y}(\text{Ti}_x\text{Zr}_{1-x})\text{B}_2$ eutectics. These compositions are presented in Figure 2 in a $\text{TiB}_2\text{-LaB}_6\text{-ZrB}_2$ ternary phase diagram and compared with the nominal composition of the starting materials. For all the rods, the regions with eutectic compositions were richer in diboride than the corresponding starting materials. This is due to the fact that the LaB_6 rich belts in the solidified rods were not taken into account in these WDX analyses. The fraction of titanium in $(\text{Ti}_x\text{Zr}_{1-x})\text{B}_2$ fibers were lower for the eutectic composition than for the starting material. Evaporation from the melt zone of titanium monoxide during the growth process could explain these differences.

The variation of the diboride fraction y in the $\text{LaB}_6\text{-y}(\text{Ti}_x\text{Zr}_{1-x})\text{B}_2$ eutectics as a function of x , did not follow a mixing rule from the two parent eutectics $\text{LaB}_6\text{-ZrB}_2$ ($y = 0.324$ for $x = 0$) [3] and

LaB₆-TiB₂ ($y = 0.246$ for $x = 1$) [16]. For $x = 0.51, 0.44$ and 0.32 , the diboride molar fraction was higher than for $x = 0$. This result is in agreement with results of Y. Paderno et al. [14] who reported a higher volume content of fibers up to $x = 0.6$ in the LaB₆-y(Ti_xZr_{1-x})B₂ eutectic composites than in LaB₆-ZrB₂ eutectic composite ($x = 0$).

Local variations in Zr and Ti concentration inside the fibers have been investigated by STEM-EDX. A typical chemical profile recorded across a diboride fiber is shown in Figure 1c. The Ti to Zr ratio was constant all over the fiber cross-section and very close to the average ratio measured by WDX. The concentrations of Ti and Zr in the LaB₆ matrix were below our detection limit (0.1% wt).

Lattice parameters of the (Ti_xZr_{1-x})B₂ fibers have been deduced from X-ray diffraction diagrams in the Bragg-Brentano geometry for which the sole diffracting planes were those lying parallel to the cross section plane. These diffracting planes could be assigned to primitive cubic LaB₆ (JCPDS file No. 34-427) and hexagonal ZrB₂ (JCPDS file No. 34-423) with a gradual shift to higher angles of the diboride diffraction peaks with increasing x . The quasi linearly decrease of the cell parameters of the diboride phase with increasing x is shown in Figure 3. The decrease rate of the c -parameter was about twice that of the a -parameter, respectively of 8.4% and 4.4%. When the radius of metal cation decreased ($r_{Zr} = 0.160$ nm, $r_{Ti} = 0.146$ nm), the contraction along a -axis was hindered due to the strong B-B bonds in the boron layers parallel to (0001), whereas the contraction along c -axis was easier due to the more ionic character of the Me-B bonds [17]. The B-B bond lengths was assumed to decrease linearly between the known values for $x = 0$ (0.1827 nm) and for $x = 1$ (0.1749 nm) i.e. to follow the same relative variations as that of the a -parameter (4.4%). The lowest misfit between the two boron sublattices was found for $x = 0.76$, the B-B bond length (0.1760 nm) was close to the intra-octahedral B-B distance in the LaB₆ structure (0.1766 nm).

3.2 Growth direction of LaB₆-y(Ti_xZr_{1-x})B₂

LaB₆-y ZrB₂ rods

Figures 4a to 4d show the (0001)₂, {10 $\bar{1}$ 1}₂-pole figures of ZrB₂ ($x = 0$) and {100}₆, {110}₆-pole figures of LaB₆ recorded from cross sections with a X-ray beam width of 2×2 mm². They display several orientations for LaB₆ and ZrB₂. We have assumed that the orientation giving rise to the highest diffracted signals on the pole figures (marked with red arrows) corresponds to the main orientation of the eutectic zones. This assumption is supported by the TEM observations of thin foils extracted from eutectic zones. The LaB₆/ LaB₆ interfaces that have been observed (Figure 1b), always separated regions of low mutual disorientation (about 3°). Figure 4e shows the stereographic projection plotted from these main orientations. The planes of LaB₆ or ZrB₂ parallel to cross-section plane of the rod (at the center of the stereographic projection) did not correspond to low index planes. The growth direction of the rod, defined as the rod axis, was close to the <210>₆ direction of the matrix (deviation ≈ 9°). During the solidification, the diboride fibers did not develop parallel to the rod axis but their growth axes were tilted with respect to the rod axis. The crystallographic growth axis of fibers was determined using TEM by tilting the fibre/matrix interfaces edge-on with respect to the electron beam (i.e. when the interface shows the minimum apparent thickness). For this orientation, the zone axis in the fiber corresponded to the fiber axis. The fiber axis was close to [0001]₂. This implies that the fiber

axes were tilted (about 32°) in regard to growth axis of rod. Similarly Deng et al. described a *deviation* of about 25° between $[0001]_2$ and rod axes in $\text{LaB}_6\text{-ZrB}_2$ DSE [12].

$\text{LaB}_{6-y}(\text{Ti}_x\text{Zr}_{1-x})\text{B}_2$ rods

A similar approach has been followed for eutectics cross sections with $x \neq 0$, but a tilt of the crystallographic growth axes of the fibers imposed to choose other diffracting planes for the pole figures of the diboride. Figures 5 shows, for $x = 0.51$, the $\{10\bar{1}0\}_2$, $\{11\bar{2}0\}_2$ -pole figures of $(\text{Ti}_x\text{Zr}_{1-x})\text{B}_2$, the $\{110\}_6$, $\{100\}_6$ -pole figures of LaB_6 , together with the stereographic projections plotted from the main orientations of the pole figures. Similar results were obtained for $x = 0.32, 0.44, 0.65, 0.76$. Several orientations were observed for the matrix whereas $(\text{Ti}_x\text{Zr}_{1-x})\text{B}_2$ fibers tended to adopt parallel orientations. The eutectic zones were assumed to correspond to the strongest diffracted signals. The growth direction of the matrix was close to $\langle 210 \rangle_6$ (deviation $\sim 5^\circ$) as was described for rods with $x = 0$. The high resolution TEM images of Figure 6 show that the fiber/matrix interfaces were edge-on when the fibers were in $\langle \bar{1}100 \rangle_2$ zone axes after titling the foil of about 10° with respect to the rod axis. Same crystallographic growth axes were obtained for all values of $x \neq 0$ with similar tilt angles relative to the rod axis.

These results show that the presence of titanium in melt zone has induced a 90° change in the crystallographic growth direction of the fibers from $[0001]_2$ for $x = 0$ to $\langle \bar{1}100 \rangle_2$ for $x \neq 0$. It has also increased the homogeneity in their tilt angle relative to the rod axis. The growth direction of the matrix is close to $\langle 210 \rangle_6$ regardless of x values.

3.3 Orientation relationship between matrix and fiber

The crystallographic orientation relationships for the principal orientations were determined from the stereographic projections drawn from the pole figures. Within less than 10° of misorientation, they all could be described by:

$$[001]_6 // [0001]_2 \text{ and } (110)_6 // (11\bar{2}0)_2 \text{ and } (\bar{1}10)_6 // (\bar{1}100)_2 .$$

This orientation relationship was already described for $x=0$ in the literature [7,12,13]. The presence of titanium does not modify the main orientation relationship between matrix and fibers even with the 90° tilt in the fibers crystallographic axis. This is explained by the cubic symmetry of the LaB_6 matrix.

To complete this XRD study of the mean orientation relationships, a localized investigation was undertaken by electron diffraction on cross sections. Figure 7a shows, for $x=0.65$, an electron diffraction pattern (EDP) recorded across the fiber/matrix interface, with a 12° tilt of the rod axis with respect to the electron beam. In this configuration, the fiber was oriented along $[\bar{1}100]_2$ zone axis whereas the matrix was oriented along $[\bar{1}10]_6$ zone axis. These two axes were therefore parallel. On this EDP, the $[0001]_2^*$ reciprocal (*) direction was parallel to $[001]_6^*$ (i.e. $(0001)_2 // (001)_6$). The local crystallographic orientation relationship was the same as the one derived from XRD investigations. Similar results were obtained for all eutectics with $x \neq 0$. The parallelism of the $(0001)_2$ and $(001)_6$ planes was preserved throughout all specimens. Maximum deviations were of 3° between $[\bar{1}100]_2$ and $[\bar{1}10]_6$ and of 19° between these axes and the growth directions of the rods. These observations differed from those we recorded on eutectics with $x=0$ and already described by Deng et al. [8]. ZrB_2 fibers observed in cross sections were oriented along $[0001]_2$ zone axis, which also makes the matrix oriented parallel to the $[001]_6$ zone axis.

On the corresponding EDP, the $[\bar{1}10]_6^*$ reciprocal direction was parallel to $[\bar{1}100]_2^*$. This confirms the change in the fiber crystallographic axes for eutectics with $x \neq 0$ with regard to eutectics with $x=0$ and the similarity between the crystallographic orientation relationships for all x values.

3. Fiber/matrix interface

TEM observations of the eutectic zone show that, for all compositions, most fibers grew faceted (Figure 1a). The main faceted interfaces between fibers and matrix observed by HRTEM are illustrated in Figure 6. The fibers and matrix were close to $[\bar{1}100]_2$ and $[\bar{1}10]_6$ zone axes respectively, as shown by Fourier Transforms. Fiber/matrix interfaces were edge-on with this orientation of the thin foil. For eutectics with $x \neq 0$ the dominant facets corresponded to $(0001)_2$ facing $(001)_6$ (Figures 6a,b,c). Facets with $(11\bar{2}0)_2$ facing $(110)_6$ (Figure 6d) have also been observed, they were less frequent and had shorter lengths.

To compare the stability of these two types of facets observed experimentally, a 2-D NCSL model was used, that considers the coincidence sites between the two lattice planes contacting at the interface. A 2-D σ index (vs. Σ , in 3-D) is introduced. To keep the consistency with the work of Deng et al [12], σ refers to the diboride lattice and is therefore defined as :

$$\sigma = \frac{A_{NSCL,2}}{A_2}$$

where $A_{NSCL,2}$ represents, in the diboride lattice, the area of the smallest cell for the 2D coincidence site lattice, and A_2 the area of the diboride cell.

To describe the misfit between the two NSCL cells drawn in the hexa- and di-boride lattices, a volume strain ε_s is introduced [12], defined as

$$\varepsilon_s = \frac{|A_{NSCL,2} - A_{NSCL,6}|}{A_{NSCL,2}}$$

Table 3 lists the vectors of the smallest NCSL (2D) cell, values of σ and ε_s for the $(11\bar{2}0)_2/(110)_6$ facets (referred to $(110)_6$) and $(0001)_2/(001)_6$ facets (referred to $(001)_6$). Figure 8 illustrates the 2D-NCSL cells for $(11\bar{2}0)_2/(110)_6$ interface planes. For all values of x , the values of σ and ε_s are lower for the $(001)_6$ facets ($\sigma=2$ and ε_s varies from 0.007 to 0.07) than for the $(110)_6$ facets ($\sigma=6$ or 5 , and ε_s varies from 0.03 to 0.12). From such a geometrical model, the $(001)_6$ facets would be more favorable than $(110)_6$ ones, which is in agreement with the TEM observations for $x \neq 0$. For $\text{LaB}_6\text{-ZrB}_2$ eutectics ($x=0$), the $(001)_6$ facets cannot develop given the growth direction of the fibers along $[0001]_6$. In this case, $(11\bar{2}0)_2/(110)_6$ facets ($\sigma=6$) and $(1\bar{1}00)_2/(1\bar{1}0)_6$ facets ($\sigma=12$) were reported [12], the former prevailing in number over the latter.

Lattice fringe images of curved interfaces exhibit ledges alternating low and high energy facets. The mechanism of lattice accommodation of the two phases at the interface can be made by a succession of dislocations, the periodicity of which depends on the orientation relationship and the interface orientation. Consequently, the fiber/matrix interfaces are semi-coherent regardless of x values.

These results show clearly that the addition of titanium in $\text{LaB}_6\text{-ZrB}_2$ composite has modified the growth direction of fibers and hence the structure of fiber/matrix interfaces. It should be mentioned that all composites are prepared in identical conditions. The alteration of crystallographic orientation of the fibers is not yet fully understood. It could be related to non-geometrical issues, such as changes in mass and momentum transport of melt with dopant additions since dopants do change the kinematic viscosity of the melt, with concurrent changes of density. Yet, the elucidation of their impact on the growth mechanism is beyond the scope of this work. In addition, charge interactions at the interface must play a significant role since the bonding nature and the electronic properties in TiB_2 and ZrB_2 are different [18].

Electron Energy Loss Spectroscopy (EELS) is a dedicated tool to investigate locally the electronic structure and coordination sphere of boron atoms in boride crystals [19]. EELS has been used in this study to detect changes in boron bonding in the fibers resulting from titanium additions. Energy Loss Near Edge Structures (ELNES) spectra, that probe the density of empty state above the Fermi level, were acquired at B_K ionization edge in $\text{Zr}_{1-x}\text{Ti}_x\text{B}_2$ ($x=0$ to 0.76) with an energy resolution of 0.8 eV (Figure 9). Same experimental conditions and crystallographic zone axis were used to eliminate the orientation-dependent ELNES effect encountered in anisotropic structures. Clear differences are seen in the spectra with and without Ti addition even for the lowest $x=0.15$ and a continuous evolution of B K-edge ELNES structures with the increase of Ti content is revealed. This shows that Ti affects the bonding configuration of boron in the fiber by a change of the local crystallographic and/or chemical environment. At present time, comparison between experiments and simulations are in progress in order to understand the arrangement of Ti atoms in the hexagonal lattice of the fibres as a function of the x value. An in-depth research in this direction will be carried out on the next stage of our studies in order to establish the structural arrangement and electronic structure at the interface.

4. Conclusion

The influence of zirconium substitution by titanium on growth direction and interface structure in $\text{LaB}_6\text{-Ti}_x\text{Zr}_{1-x}\text{B}_2$ ($x=0.32$ to 0.76) directionally solidified ceramics has been studied and the following conclusions have been drawn:

1°) The diboride molar fraction at the eutectic invariant point can be determined more precisely using WDX for each of the composition with $0.32 \leq x \leq 0.76$. The $\text{LaB}_6\text{-Ti}_x\text{Zr}_{1-x}\text{B}_2$ eutectic compositions do not follow a rule of mixture from the parent eutectics, $\text{LaB}_6\text{-ZrB}_2$ and $\text{LaB}_6\text{-TiB}_2$. Lattice parameters of $\text{Ti}_x\text{Zr}_{1-x}\text{B}_2$ solid solutions obey a Vegard's law.

2°) Titanium addition caused alteration of fiber growth directions. The fibers grew along $\langle \bar{1}100 \rangle_2$ for $\text{LaB}_6\text{-(Ti}_x\text{Zr}_{1-x})\text{B}_2$ with $x \neq 0$ against $[0001]_2$ for $\text{LaB}_6\text{-ZrB}_2$. The fibers axes were tilted with respect to the rod axis of around 10° for $x \neq 0$ and 30° for $x=0$. The growth direction of the matrix remained the same, and was close to $\langle 210 \rangle_6$.

3°) The introduction of titanium did not influence the crystallographic orientation relationship between matrix and that remains close to:

$[001]_6/[0001]_2$ and $(110)_6/(11\bar{2}0)_2$ and $(\bar{1}10)_6/(\bar{1}100)_2$.

4°) The $\text{Ti}_x\text{Zr}_{1-x}\text{B}_2$ fibers developed faceted interfaces. $(0001)_2/(001)_6$ facets were the most frequent ones, before $(11\bar{2}0)_2/(110)_6$ ones. A 2D near coincidence site lattice model adequately explained the facet stability from a geometrical point of view. The (001) facets were found to be more stable ($\sigma=2$) than the (110) ones ($\sigma=5$ or 6). In $\text{LaB}_6\text{-ZrB}_2$ eutectics, $(0001)_2/(001)_6$ facets cannot develop since the fiber axis is $[0001]_6$. Titanium addition may result in an interface energy reduction. Quantum mechanical and ab-initio calculations are required to validate this conclusion.

References

1. V.N. Paderno, Y.B. Paderno, V.B. Filipov and B.A. Arkhipov, "The working reliability and structure stability of thermoemission lanthanum hexaboride elements in stationary plasma thruster hollow cathodes", *J. Mater. Process. Manu. Sci.*, 6 [4] 311-320 (1998).
2. V.I. Lazorenko, D.V. Lotsko, V.F. Platonov, A.V. Kovalev, A.P. Galasun, A.A. Matvienko and A.E. Klinkov, "Oriented growing and anisotropy of the emissive properties of lanthanum hexaboride single crystals", *Sov. Powder. Metall.*, 26 [3] 51-57 (1987).
3. Y. Paderno, V. N. Paderno, V. B. Filipov, Yu. V. Mil'man and A. N. Martynenko, "Structure features of the eutectic alloys of borides with the d- and f-transition metals", *Powder Metall. Met. C+*, 31 [8] 700-706 (1992).
4. C.-M. Chen, L.T. Zhang and W.C. Zhou, "Characterization of $\text{LaB}_6\text{-ZrB}_2$ composite grown by the floating zone method", *J. Cryst. Growth*, 191, 873-878, (1998).
5. I. Bogomol, T. Nishimura, Y. Nesterenko, O. Vasylykiv, Y. Sakka and P. Loboda, "The bending strength temperature dependence of the directionally solidified eutectic $\text{LaB}_6\text{-ZrB}_2$ composite", *J. Alloy. Compd.*, 509 [20] 6123-6129 (2011).
6. Y. Paderno, 'A new class of 'in-situ' fiber reinforced boride composite ceramic materials'; pp. 353–369 in *Advanced Multilayered and Fiber-Reinforced Composites*, Edited by Y. M. Haddad, Kluwer Academic Publishers, The Netherlands, 1998
7. Y. Paderno, V. Paderno and V. Filipov, 'Crystal chemistry of eutectic growth of d- and f-transition metals borides', in *Proc. 11th Int. Symp. Boron, Borides and Related Compounds*, Tsukuba, 1993, JJAP series [10] 190-193 (1994).
8. H. Deng, E.C. Dickey, Y. Paderno, V. Paderno, V. Filipov and A. Sayir, "Crystallographic characterization and indentation mechanical properties of $\text{LaB}_6\text{-ZrB}_2$ directionally solidified eutectics", *J. Mater. Sci.*, 39 [19] 5987-5994 (2004).
9. H. Deve and M.J. Maloney, "On the toughening of intermetallics with ductile fibers: role of interfaces", *Acta Metall. Mater.*, 39 [10] 2275-2284 (1991).
10. C.-H. Chen, T. Aizawa, N. Iyi, A. Sato and S. Otani, "Structural refinement and thermal expansion of hexaborides", *J. Alloy. Compd.*, 366 [1-2] L6-L8 (2004).
11. K.E. Shear, "Chemical bonding in AlB_2 -type borides", *J. Less-Common Met.*, 47 195-201 (1976).
12. H. Deng, E.C. Dickey, Y. Paderno, V. Paderno and V. Filipov, "Interface crystallography and structure in $\text{LaB}_6\text{-ZrB}_2$ directionally solidified eutectics", *J. Am. Ceram. Soc.*, 90 [8] 2603-2609 (2007).

- 13 C.-M. Chen, W.-C. Zhou and L.-T. Zhang, “Oriented structure and crystallography of directionally solidified $\text{LaB}_6\text{-ZrB}_2$ eutectic”, *J. Am. Ceram. Soc.*, 81 [1] 237-240 (1998).
- 14 Y. Paderno, V. Paderno and V. Filipov, “Some peculiarities crystallization of $\text{LaB}_6\text{-(Ti,Zr)B}_2$ alloys”, *J. Solid State Chem.*, 154 [1] 165-167 (2000).
- 15 S. Otani, T. Aizawa and N. Kieda, “Solid solution ranges of zirconium diboride with other refractory diborides: HfB_2 , TiB_2 , TaB_2 , NbB_2 , VB_2 and CrB_2 ”, *J. Alloy. Compd.* 475 [1-2] 273-275 (2009).
- 16 V. Filipov, PhD Thesis, Institute for Problems of Materials Science, National Academy of Sciences of Ukraine, Kyiv, April 2007.
- 17 X. Zhang, X. Luo, J. Han, J. Li, W. Han “Electronic structure, elasticity and hardness of diborides of zirconium and hafnium: First principles calculations” *Comp. Mater. Sci.*, 44 [2] 411–421 (2008)
- 18 H.Y. Wang, F.Y. Xue, H. Zhao, D.J. Li “First-Principles Calculation of Elastic Properties of TiB_2 and ZrB_2 ” *Adv. Mater. Res.* 150-151, 40-43 (2011)
- 19 K. Hofmann, R. Gruehn, B. Albert Prof, “Probing for Structural Features of Boron-rich Solids with EELS”, *Z. Anorg. Allg. Chem.* 628 [12] 2691–2696 (2002).

Tables

Table 1. Nominal compositions of the starting materials used for the directional solidification of the eutectic rods.

x in $\text{Ti}_x\text{Zr}_{1-x}\text{B}_2$	y $\text{LaB}_{6-y}(\text{Ti}_x\text{Zr}_{1-x}\text{B}_2)$
atomic fraction	mol fraction
0	0.32
0.4	0.314
0.5	0.317
0.6	0.309
0.7	0.287
0.8	0.289

Table 2. Composition of $\text{LaB}_{6-y}(\text{Ti}_x\text{Zr}_{1-x}\text{B}_2)$ composites in the eutectic regions, as determined by EPMA.

x in $\text{Ti}_x\text{Zr}_{1-x}\text{B}_2$	y $\text{LaB}_{6-y}(\text{Ti}_x\text{Zr}_{1-x}\text{B}_2)$
atomic fraction	mol fraction
0	0.302
0.32	0.362
0.44	0.358
0.51	0.348
0.65	0.309
0.76	0.298

Table 3. NCSL(2D) cell analysis of (110)-LaB₆//($11\bar{2}0$)-Ti_xZr_{1-x}B₂ and (001)-LaB₆//(0001)-Ti_xZr_{1-x}B₂ facets as a function of x (tolerance factor <0.05 nm).

	(110)//($11\bar{2}0$) facet planes		(001)//(0001) facet planes				
x	0, 0.32	0.44, 0.51, 0.76	0	0.32	0.44	0.51	0.76
NCSL _{LaB₆}							
u' ₁	[1-10]	[1-14]	[110]	[110]	[110]	[110]	[110]
u' ₂	5×[001]	4× [001]	[320]	[430]	[540]	[540]	[650]
NCSL _{Ti_xZr_{1-x}B₂}							
u ₁	[1-1.0]	[1-1.5]	2[11.0]	2[11.0]	2[11.0]	2[11.0]	2[11.0]
u ₂	6×[00.1]	5×[00.1]	[54.0]	[76.0]	[98.0]	[98.0]	2[11 10. 0]
σ	6	5	2	2	2	2	2
ε _s	0.03, 0.09	0.06, 0.08, 0.12	0.007	0.03	0.04	0.04	0.07

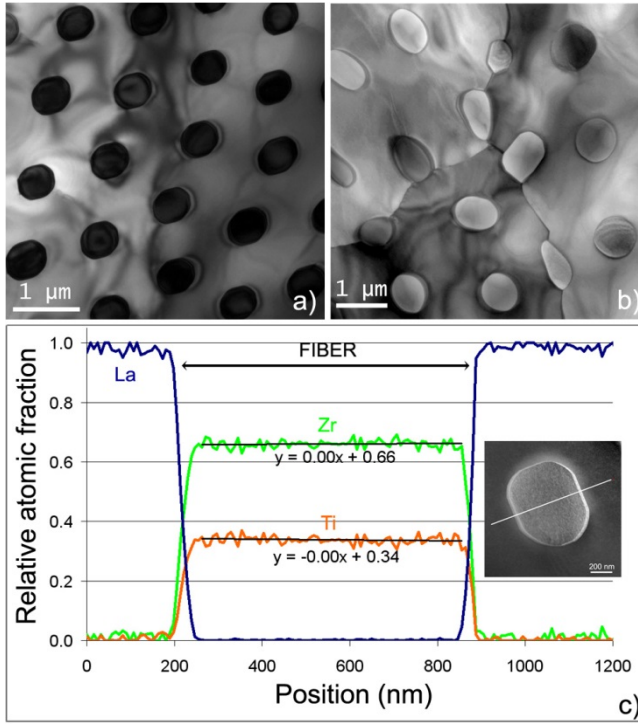


Fig 1. (a) Bright field TEM images of LaB₆-y(Ti_xZr_{1-x})B₂ composite showing a uniform zone at the centre of rod. The fibers are tilted with respect to rod axis. Their mean diameter (smallest diameter of the section) is 0.6 μm. (b) matrix grain boundaries of low angular disorientation and (c) STEM-EDX profile across a single fiber giving its relative atomic fractions for La, Zr and Ti. An electron probe of 2 nm in diameter and an analysis step of 8 nm were used. The tendency lines show that the Zr and Ti relative fractions in the fiber cross section are almost constant and correspond to x = 0.34, close to the value x = 0.32, measured by WDX.

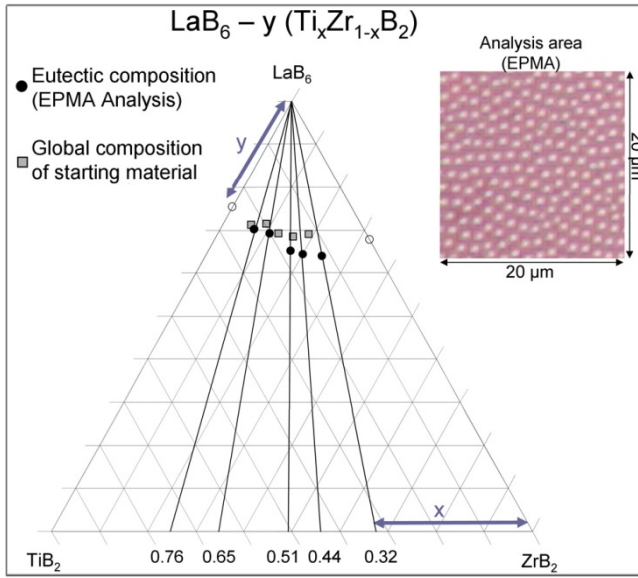


Fig 2. $\text{LaB}_6\text{-TiB}_2\text{-ZrB}_2$ ternary phase diagram: ■ global compositions determined from starting material; ● eutectic compositions determined by EPMA; ○ eutectic compositions in binary systems: $\text{LaB}_6\text{-ZrB}_2$ [3] and $\text{LaB}_6\text{-TiB}_2$ [16]. (insert: optical microscope image typical of a eutectic area analyzed by EPMA).

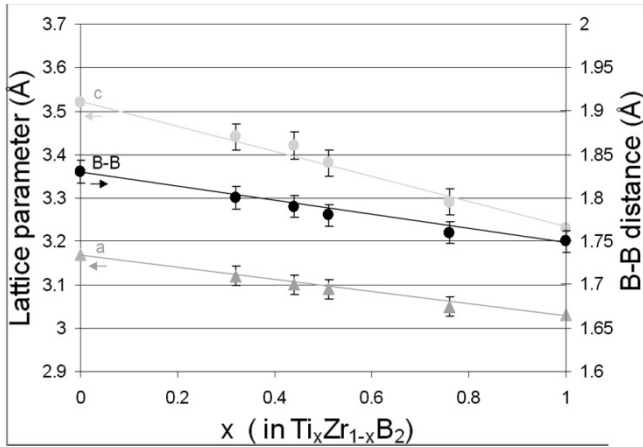


Fig 3. Variation of the lattice parameters of the $(\text{Ti}_x\text{Zr}_{1-x})\text{B}_2$ fibers as a function of x determined from X-Ray diffraction diagrams. The continuous line is plotted from lattice parameters of TiB_2 and ZrB_2 structures.

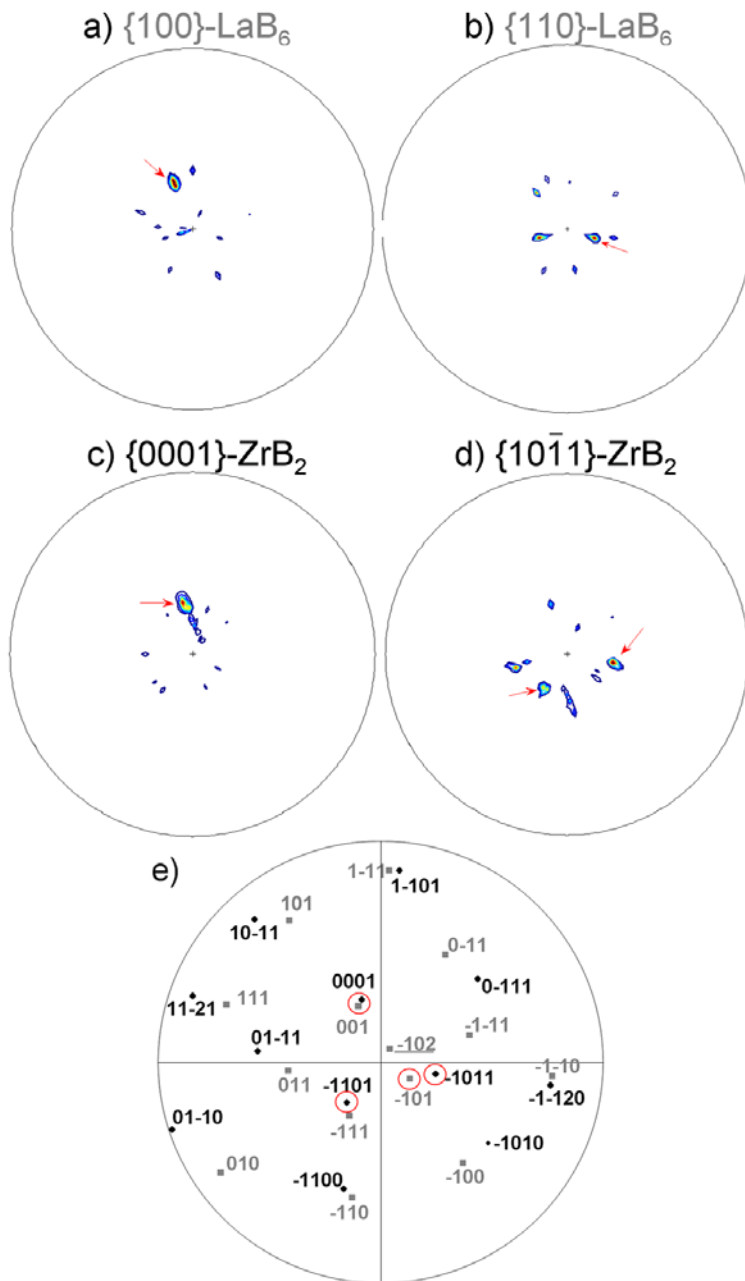


Fig 4. $\text{LaB}_6\text{-ZrB}_2$ composite ($x = 0$).

a) to d) X-ray pole figures of $\{001\}$, $\{110\}$ for LaB_6 and $\{0001\}$, $\{10\bar{1}1\}$ for ZrB_2 .

e) stereographic projection built from main orientations of a,b,c,d pole figures (indexation of poles: \blacklozenge for ZrB_2 ; \blacksquare for LaB_6).

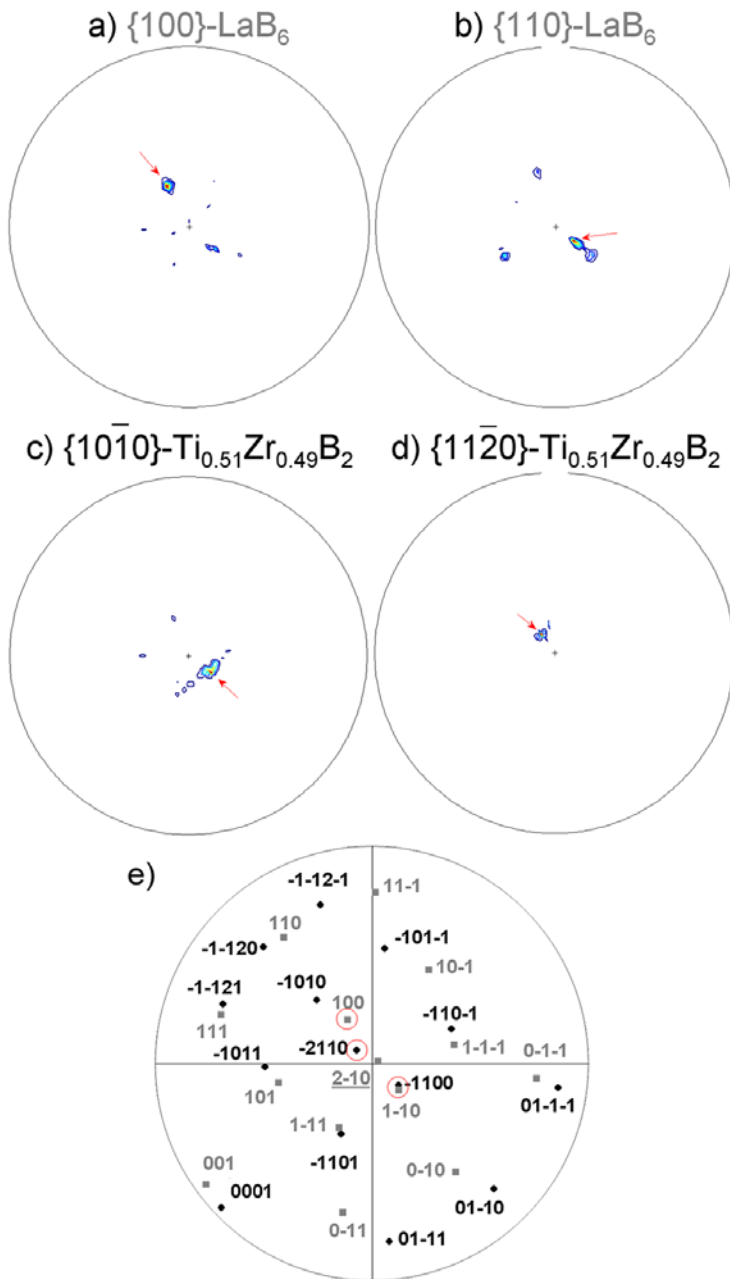


Fig 5. $\text{LaB}_6\text{-Ti}_{0.51}\text{Zr}_{0.49}\text{B}_2$ composite :

a) to d) X-ray pole figures of $\{001\}$, $\{110\}$ for LaB_6 and $\{10\bar{1}0\}$, $\{11\bar{2}0\}$ for $\text{Ti}_{0.51}\text{Zr}_{0.49}\text{B}_2$
e) stereographic projection built from main orientations of a,b,c,d pole figures (indexation of poles: \blacklozenge for $\text{Ti}_{0.51}\text{Zr}_{0.49}\text{B}_2$; \blacksquare for LaB_6).

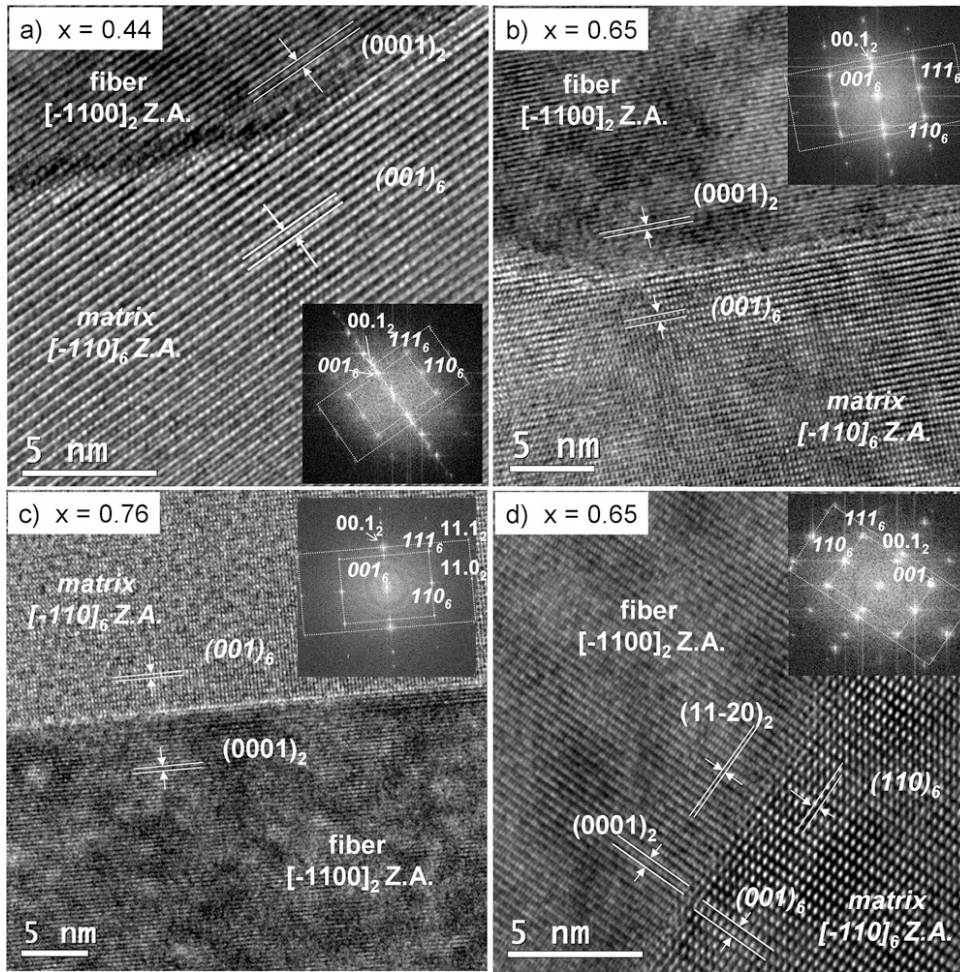


Fig 6. HRTEM images of faceted fiber/matrix interfaces with the interface plane parallel to (001) for (a) $x = 0.44$; (b) $x = 0.65$ (c) $x = 0.76$ and (d) with the interface plane parallel to (110) for $x = 0.65$. The Fast Fourier Transforms of the images are added.

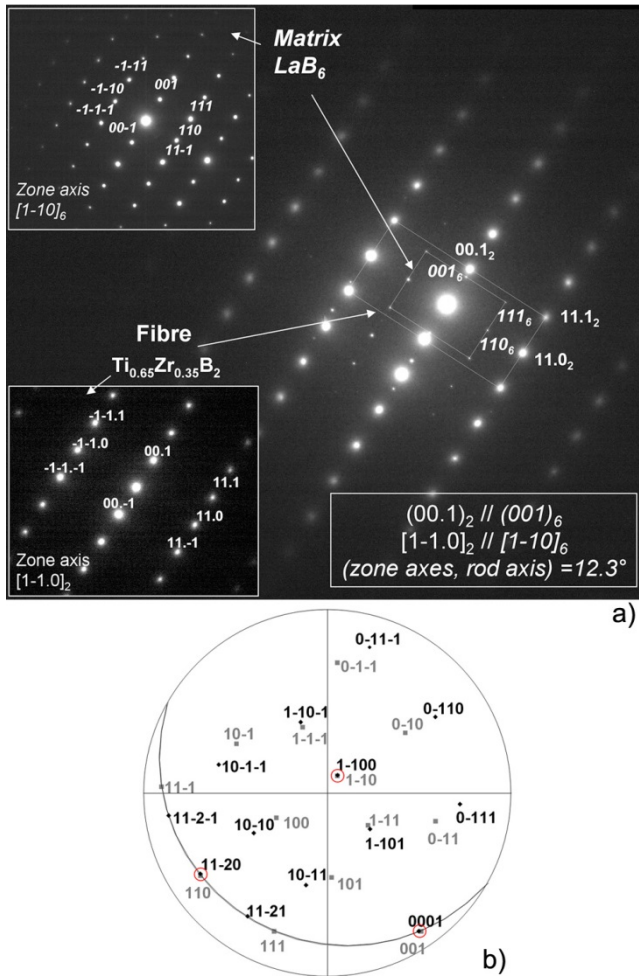


Fig 7. a) Electron diffraction (ED) patterns obtained along $[\bar{1}\ 100]$ - $\text{Ti}_{0.65}\text{Zr}_{0.35}\text{B}_2$ and $[\bar{1}\ 10]$ - LaB_6 zone axes; b) stereographic projection built from tilt angles of ED patterns. The two great circles corresponding to the matrix and fiber orientations in the HRTEM image are drawn (indexation of poles: \blacklozenge for $\text{Ti}_{0.65}\text{Zr}_{0.35}\text{B}_2$; \blacksquare for LaB_6).

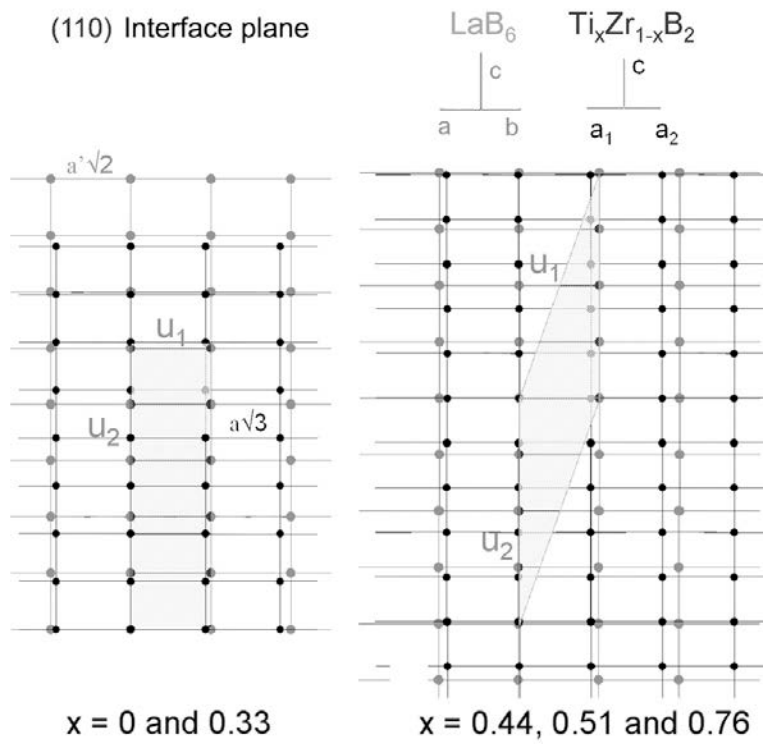


Fig 8. Projections of NCSL (2D) as a function of x in the (110) interface plane.

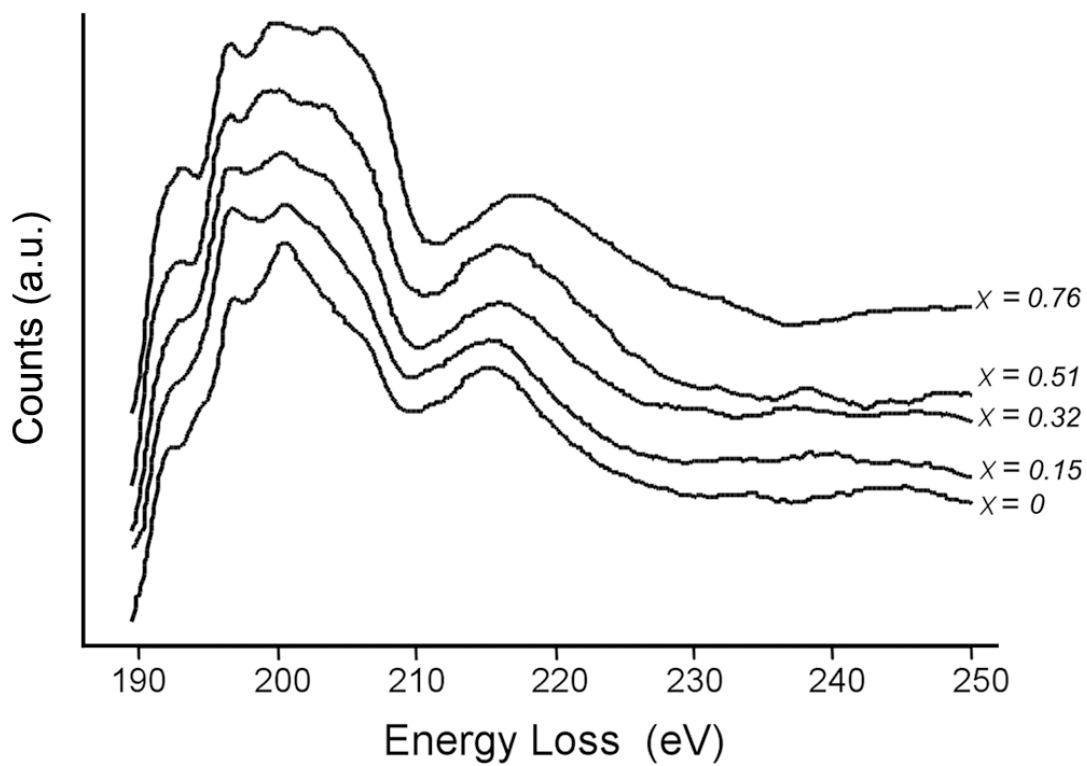


Fig 9. EELS spectra of the K absorption edge of boron for $x=0$, 0.15 (added for more clarity), 0.32, 0.51 and 0.76.

Thermophysical Properties of Undoped and Doped $(\text{Ti}_{0.75}\text{Sn}_{0.25})\text{O}_2$

Executive Summary

Eutectics are multiphase structures formed by the cooperative growth of two or more phases. Although the internal structure can vary widely, the development of continuous rods or plates in a matrix can be achieved and, within limits, can be controlled or “tailored” through directional solidification. This self-assembly structure provided a pathway over the years to design superior aeronautical structures with integrated functionalities, such as piezoelectric actuators (ferroelectricity), hydrogen membranes (proton conductors) and power generation (thermoelectricity) that created a synergic composites. While experimental investigations of multifunctional polyphase structures using directional solidification have been particularly successful, our understanding of the fundamental nature of the polyphase structures has been fairly monotonic. In first year of our project we focused on the formation of nanostructures by self-assembly that take advantage of thermodynamic equilibrium of spinodal decompositions to produce stable nanostructures with coherent interfaces. The thermoelectric properties of undoped and doped $(\text{Ti}_{0.75}\text{Sn}_{0.25})\text{O}_2$ were investigated for high-temperature thermoelectric conversion application. Nanocomposites were formed by annealing above 1000 °C. Outside the spinodal dome, metastable ilmenite-type SnTiO_3 precipitated from the rutile structure. Thermoelectric properties were measured in the temperature range from room temperature to 1000 °C. $(\text{Ti}_{0.75}\text{Sn}_{0.25})\text{O}_2$ was doped with both acceptor and donor dopants. Both undoped and doped $(\text{Ti}_{0.75}\text{Sn}_{0.25})\text{O}_2$ exhibit n-type electrical behavior. The electrical conductivity, σ , was enhanced three orders of magnitude by doping with Nb_2O_5 or Ta_2O_5 ; achieving 546 S/m at 850 °C. The increased in electrical conductivity was accompanied by reduction of the absolute Seebeck coefficient, S . Absolute Seebeck value decreased by -600 mV/K from undoped to 4% Ta_2O_5 doping. The solid solution and doping reduced the thermal conductivity, k , to <4 W/mK, far below the parent materials TiO_2 and SnO_2 . Lattice thermal conductivity decreased with increasing temperature, achieving 1.9 W/mK at 900 °C for 4% Ta_2O_5 doping. No further reduction in thermal conductivity was observed in annealed samples containing nano-sized SnTiO_3 precipitates. Dimensionless figure of merit (ZT) attained was less than 0.1.

Coherent Interface Structure of (Ti_{0.75}Sn_{0.25})O₂ System

Nanostructures formed by self-assembly take advantage of thermodynamic equilibrium to produce stable nanostructures with coherent interfaces. The SnO₂-TiO₂ system exhibits spinodal decomposition as shown in Fig. 1. The composition range is large; the phase separated structure can be stable up to 1450 °C. Nanostructure morphology is dependent upon the Ti/Sn ratio and thermal path. Periodic fluctuation of composition and lamellae structure are obtained inside the spinodal dome centered near the equimolar composition. Nano-precipitates are obtained by nucleation and growth in between the miscibility gap and spinodial region. In the spinodal dome, small delocalized fluctuation of composition is amplified into periodic modulations, as shown in Fig. 2. Due to anisotropic elastic coefficients, the spinodal structures tend to be aligned along elastically soft directions. This produces a sequence of Ti rich and Sn rich rutile lamellae parallel to (001) planes with coherent interfaces (Fig. 2). High temperature annealing is necessary to overcome kinetic limitations for decomposition. In addition to temperature, the spinodal decomposition rate can be enhanced by acceptor cation doping and inhibited by donor cation doping. [5-8] Spinodal decomposition has been widely studied but limited information is reported on the (Sn_xTi_{1-x})O₂ alloy properties and the nucleation and growth region.

The (Sn_xTi_{1-x})O₂ system is ideal for fabrication of thermodynamically stable nanostructures and potential pathway in reduction of thermal conductivity. The large mass difference between Ti and Sn disrupts phonon conduction. The lamellar structure with periodic spacing can be effective in scattering phonons, the magnitude of scattering being dependent upon the lamellae width. The decrease in thermal conductivity by partitioning into lamellae or nanoparticles is known for semiconductor systems, leading to high ZT thermoelectric materials.

TiO₂ and SnO₂ have the same crystal structure but exhibit different electrical behavior. The conduction band of TiO₂ is composed of localized 3d orbitals, conduction occurs by either small or large polaron hopping. The d and p band character in TiO₂ limits the mobility of electrons. The s and p band character of SnO₂ provides larger electron mobility. The admixing Sn 5s states to the TiO₂ matrix should be beneficial to electrical transport.

Undoped and doped compositions of (Sn_{0.25}Ti_{0.75})O₂ were prepared by conventional solid state reaction from stoichiometric amounts of SnO₂(MTI Corp.) and TiO₂(MTI Corp.) powders. Metal oxide dopants used were Ta₂O₅(Inframat), Nb₂O₅(Inframat), In₂O₃(MTI Corp.), Sb₂O₃(MTI Corp.), MnO(Alpha Aesar), and CoO(Alpha Aesar). Purity level of the powders was 99.9% or greater. The powders were prepared by wet milling SnO₂ and TiO₂ in isopropyl alcohol for 24 hrs. using polypropylene jars with yttrium stabilized zirconia balls. After drying, the powders were pressed into pellets (32.0 mm x 2.0 mm) by uniaxial pressing (20 MPa) in a steel die. The pellets were then sintered at 1550 °C, using a heating rate of 5 °C/min, soaked for 2 hrs. in ambient atmosphere and cooled to room temperature at a rate of 5 °C/min.

The microstructure of sintered pellets was characterized by scanning electron microscopy (SEM) and transmission electron microscopy (TEM). For thin-foil preparation, cylindrical specimens of 3 mm diameter were cut by an ultrasonic disc cutter. These cylinders were processed into TEM foils by tripod[®] polishing followed by argon ion milling at 4 kV for 10 min to obtain a thickness

less than 100 nm. Prepared samples were examined with a 200kV FEG-TEM-STEM (Tecnai F20 ST) equipped with a high angular annular dark field detector (HAADF) and an EDX spectrometer. Secondary phase was determined by the EDS stage attached to the TEM and electron diffraction.

The samples for the thermoelectric property measurements were fabricated from the sintered samples in the form of rectangular bars (~ 3 mm x 3 mm x 15 mm). The direct-current (DC) conductivity (σ) and Seebeck coefficient (S) were measured jointly using ZEM-3 (ULVAC, Japan) in the temperature range of 100°–1000°C. Measurements were done in a partial vacuum containing helium (0.021 MPa); a constant pressure of oxygen was not maintained during the measurement. Thermogravimetric analysis showed a weight loss of 0.1% under measurement conditions. The DC four-probe technique was utilized to measure electrical conductivity. A temperature gradient (DT) was achieved by heating one end of the sample. The Seebeck coefficient was calculated from the linear slope of voltage versus temperature (DV/DT); the measurement compensated for the Seebeck voltage in the measurement wires.

Thermal conductivity (k) and specific heat of the polycrystalline samples were measured using the laser-flash method (Flashline 5000, Anter Corp.) from room temperature to 1000°C in nitrogen environment. Both sides of the sample were coated with a 1 mm Pt coating by physical vapor deposition. A graphite coating was applied on top of the Pt coating by aerosol spray. At each measurement temperature, three laser shots were used to obtain the average thermal diffusivity. A reference sample was used in each measurement for determination of specific heat. Thermal conductivity was determined from the average thermal diffusivity, heat capacity and sample density.

Fig. 3 shows the sintered microstructures of undoped and doped $(\text{Ti}_{0.75}\text{Sn}_{0.25})\text{O}_2$. Undoped $(\text{Ti}_{0.75}\text{Sn}_{0.25})\text{O}_2$ sinters to high density at 1550 °C (Fig. 3A). Significant grain growth occurs during sintering, resulting in an average grain size of 20.9 mm. The $(\text{Ti}_{0.75}\text{Sn}_{0.25})\text{O}_2$ average grain size is similar to 25.1 mm reported by Beuno et al. for samples sintered at 1450 °C. The high TiO_2 content dominated sintering behavior. Densification dependence on TiO_2 content has been reported,[12] where the higher TiO_2 content improves densification and increases the mean grain size. When SnO_2 dominates sintering, densification is problematic due to Sn evaporation and surface diffusion at high and low temperatures, respectively. Doping with a +2 cation such as Mn or Co is required for successful densification.

Six dopants, three donors (Nb_2O_5 , Ta_2O_5 , Sb_2O_5) and three acceptors (In_2O_3 , CoO , MnO), were investigated to modify the microstructure and electrical properties of $(\text{Ti}_{0.75}\text{Sn}_{0.25})\text{O}_2$. Two of the donor dopants (Nb_2O_5 and Sb_2O_5) resulted in lower sintered densities. Nb_2O_5 doped specimens (Fig. 3c) exhibited larger grain sizes with a large population of pores at the grain boundaries and triple points than undoped samples. Average grain size for 1% and 4% Nb_2O_5 additions were 6.3 mm and 22.8 mm, respectively. Samples containing 4% Nb_2O_5 were mechanically fragile. Similarly, successful densification was not achieved with Sb_2O_5 doping of 1 - 4 mole %. Further investigation into inhibited densification by Sb_2O_5 doping was not pursued. The addition of Ta_2O_5 to $(\text{Ti}_{0.75}\text{Sn}_{0.25})\text{O}_2$ suppressed grain growth as shown in Fig. 3B but did not impede densification. Ta_2O_5 addition up to 4% produced finer grain microstructures with the following average grain sizes: (a) 0.5% Ta_2O_5 – 4.5 mm, (b) 1% Ta_2O_5 – 3.4 mm, (c) 2% Ta_2O_5 – 5.7 mm and (d) 4% Ta_2O_5 – 2.1 mm.

Acceptor dopants did not dissolve in the solid solution and precipitated at the grain boundaries. The addition of In_2O_3 did not impede densification but it promoted significant grain growth. Average grain size of 34.1 nm was observed for 1% In_2O_3 (Fig. 3D). XRD of the specimen showed In_2O_3 peaks. Electron microscopy showed a secondary phase along the grain boundaries, possibly In_2O_3 precipitation. Elemental analysis by EDX was not pursued. The addition of +2 cations, CoO or MnO , reduced the sintering temperature from 1550 °C to 1350 °C. SEM imaging by backscattered electrons showed dopant segregation along the grain boundaries, yielding a higher electrical resistivity. Cation segregation has been well documented for varistor based ceramics such as SnO_2 and TiO_2 . [15]

The remaining report is focused on $(\text{Ti}_{0.75}\text{Sn}_{0.25})\text{O}_2$ doped with Ta and Nb since they were the only dopants that produced acceptable microstructures and electrical properties. Fig. 4A shows the XRD patterns of both undoped and doped $(\text{Ti}_{0.75}\text{Sn}_{0.25})\text{O}_2$ after sintering. Except for 4% Nb_2O_5 , the XRD peaks index well with the $(\text{Ti}_{0.75}\text{Sn}_{0.25})\text{O}_2$ sample with slight peak shifts. At 4% Nb_2O_5 , the intensity of the (101) and (200) peaks are drastically reduced. None of the compositions showed any indication of spinodal decomposition, which normally appear as satellite peaks at (110) and (101) reflections [4-8]. Beuno et al. also reported no spinodal decomposition for undoped $(\text{Ti}_{0.75}\text{Sn}_{0.25})\text{O}_2$. Kinetic measurements have shown that doping with Ta_2O_5 suppresses spinodal decomposition rate. [5-7]

Specimens were annealed at 1200 °C for 72 hrs, XRD results showed no evidence of spinodal decomposition. Fig. 4B compares the XRD patterns for as sintered and annealed $(\text{Ti}_{0.75}\text{Sn}_{0.25})\text{O}_2$. New diffraction peaks were observed but the phase could not be identified from XRD database. New phase was identified as SnTiO_3 by TEM; it will be discussed later in the section. Both Ta and Nb doping follow Goldschmidt's rules of substitution for both Sn and Ti: 1) valence difference between cations is no more than one and 2) difference in the ionic radii size of substituting ions is less than 15%. Based on XRD results, Ta_2O_5 appears to have a higher solubility than Nb_2O_5 . In pure TiO_2 , phase diagrams show a higher Nb_2O_5 solubility (~10%) than Ta_2O_5 (~1%). But SnO_2 exhibits a higher Ta_2O_5 solubility than TiO_2 . Beuno et al. showed that 0.5 mole % Nb_2O_5 doped $(\text{Ti}_{0.75}\text{Sn}_{0.25})\text{O}_2$ is a low voltage varistor. Segregated phase at the grain boundary normally occur for varistors.

$(\text{Ti}_{0.75}\text{Sn}_{0.25})\text{O}_2$ doped with 1% Ta_2O_5 was examined using TEM. The microstructure was found to be dependent upon annealing conditions. No lamellae structure was observed at this high TiO_2 content. The as sintered composition exhibited a high density of dislocations as shown in Fig. 5. Domains bounded by partial dislocations were slightly disoriented with respect to the matrix, creating moiré fringes and arcs around spots on selected area diffraction (SAD) patterns. EDX profiling did not show any significant cation variations across these domains. Spot separation associated to any variation in cell lattice parameters was not observed. Therefore, it was concluded that the as sintered specimen was a solid solution.

Annealing at 950°C in air for 48 hours reduced the density of intra-granular dislocations, as shown in Fig. 6. A tweed contrast was observed. Fig. 7A shows a SAD pattern with spot separation along $[001]^*$ and diffused lines. No distinct lamellae were observed comparable to those seen in the equimolar composition (Fig. 2). Fig. 7B shows a high resolution TEM image; Fig 7C and 7D show two inversed fourier transforms generated from the split (002) spots.

Splitting occurred due to the difference in c-lattice parameter between Sn and Ti rich phases. Modulation in composition without a clear interfacial boundary is revealed by these images. At the nano-scale, composition modulation is observed to be on the order of 10 nm or less.

Annealing at 1250°C produced a microstructure containing nano-precipitates in the rutile matrix. Fig. 8A shows oriented planar precipitates in the rutile matrix that appears to resemble Guinier Preston (GP) zones. The GP segments appear darker in bright field and brighter in Z contrast images, indicating denser zones, which are assumed richer in Sn than the matrix. The SAD pattern, Fig. 8B, shows no spot splitting on hkl spots with $l \neq 0$; the platelets do not correspond to Sn rich rutile. A new set of weak spots were observed at $1/3$ and $2/3$ $[111]^*$; a few spots at almost $1/3$ and $2/3$ $[101]^*$ were also observed. Such tripling of the periodicity associated with GP zone in a rutile matrix has been reported by Banfield and Veblen for metamorphic rutile TiO_2 that contained Fe^{2+} .

The structure of the platelets determined from TEM analysis corresponded to ilmenite structure ($FeTiO_3$), i.e., hematite type structure (Fe_2O_3 isostructure of corundum) with ordering of Fe and Ti cations. The platelets were generally one or two unit cells wide as those shown in Fig. 8A; they are viewed as extended defects of rhombohedral oxide structure in rutile. Yu and Shen [] have revealed ilmenite precipitates ($SnTiO_3$) in TiO_2 - SnO_2 system that exhibited epitaxy with the rutile matrix but showed no GP zones. The epitaxial relationship between ilmenite (i) and rutile (r) is $(001)_i // (100)_r$ $[100]_i // [010]_r$. This epitaxy is favored by a fair match between the lattices with $(003)_i \sim (100)_r$ and $(110)_i \sim (101)_r$. This relationship explained the tripling of the periodicity observed along (111). In other parts of the foil, the GP zone was not observed but phase separation was clearly observed in the form of coherent Sn rich precipitates in a TiO_2 rich matrix as shown by Fig. 8C. The high resolution image shows a parallelism of the planes in the two phases. The SAD pattern, Fig. 8D, exhibited spots on a set of circles that are assigned to ilmenite. The strong crystallographic texture of the precipitates with respect to the matrix was shown by the alignment of the spots on the circles. Based on our limited results and Yu and Shen, the effect of Ta doping on the precipitation process could not be assessed.

GP zones have also been identified in Ti-doped MgO and Zr-doped Fe_2O_3 . The co-existence of GP zones and platelets suggested that the GP zone might be an intermediate step in the nucleation and growth of $SnTiO_3$. Further detailed work is required to understand the precipitation process in relation to doping, temperature and composition. Ta_2O_5 doping is known to inhibit spinodal decomposition, it is believed to inhibit diffusion of interstitial Ti.

Conclusions

The thermoelectric properties of undoped and doped $(Ti_{0.75}Sn_{0.25})O_2$ were investigated for high-temperature thermoelectric conversion application (Figures 9 through 11). Nanocomposites were formed by annealing above 1000 °C. Outside the spinodal dome, metastable ilmenite-type $SnTiO_3$ precipitated from the rutile structure. Thermoelectric properties were measured in the temperature range from room temperature to 1000 °C. $(Ti_{0.75}Sn_{0.25})O_2$ was doped with both acceptor and donor dopants. Both undoped and doped $(Ti_{0.75}Sn_{0.25})O_2$ exhibit n-type electrical behavior. The electrical conductivity, s , was enhanced three orders of magnitude by doping with Nb_2O_5 or Ta_2O_5 ; achieving 546 S/m at 850 °C. The increased in electrical conductivity was accompanied by reduction of the absolute Seebeck coefficient, S . Absolute Seebeck value

decreased by -600 mV/K from undoped to 4% Ta_2O_5 doping. The solid solution and doping reduced the thermal conductivity, k , to <4 W/mK, far below the parent materials TiO_2 and SnO_2 . Lattice thermal conductivity decreased with increasing temperature, achieving 1.9 W/mK at 900 °C for 4% Ta_2O_5 doping. No further reduction in thermal conductivity was observed in annealed samples containing nano-sized SnTiO_3 precipitates. Dimensionless figure of merit (ZT) attained was less than 0.1.

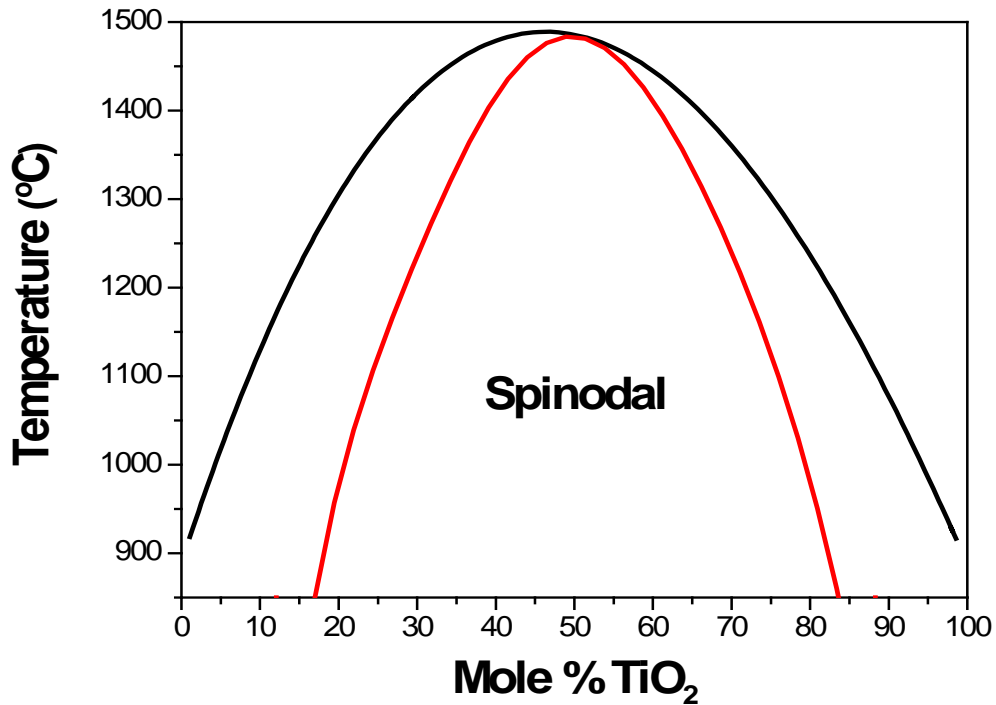


Figure 1. SnO_2 – TiO_2 phase diagram as determined by Garcia and Speidel [1].

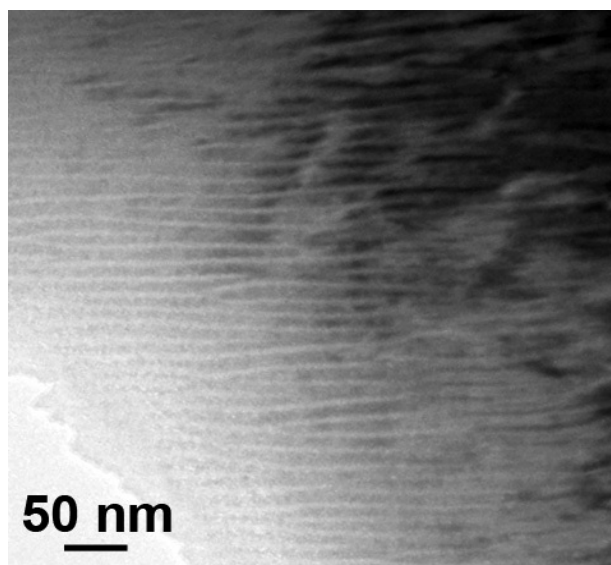


Fig. 2 Microstructure of spinodally decomposed $(\text{Ti}_{0.5}\text{Sn}_{0.5})\text{O}_3$.

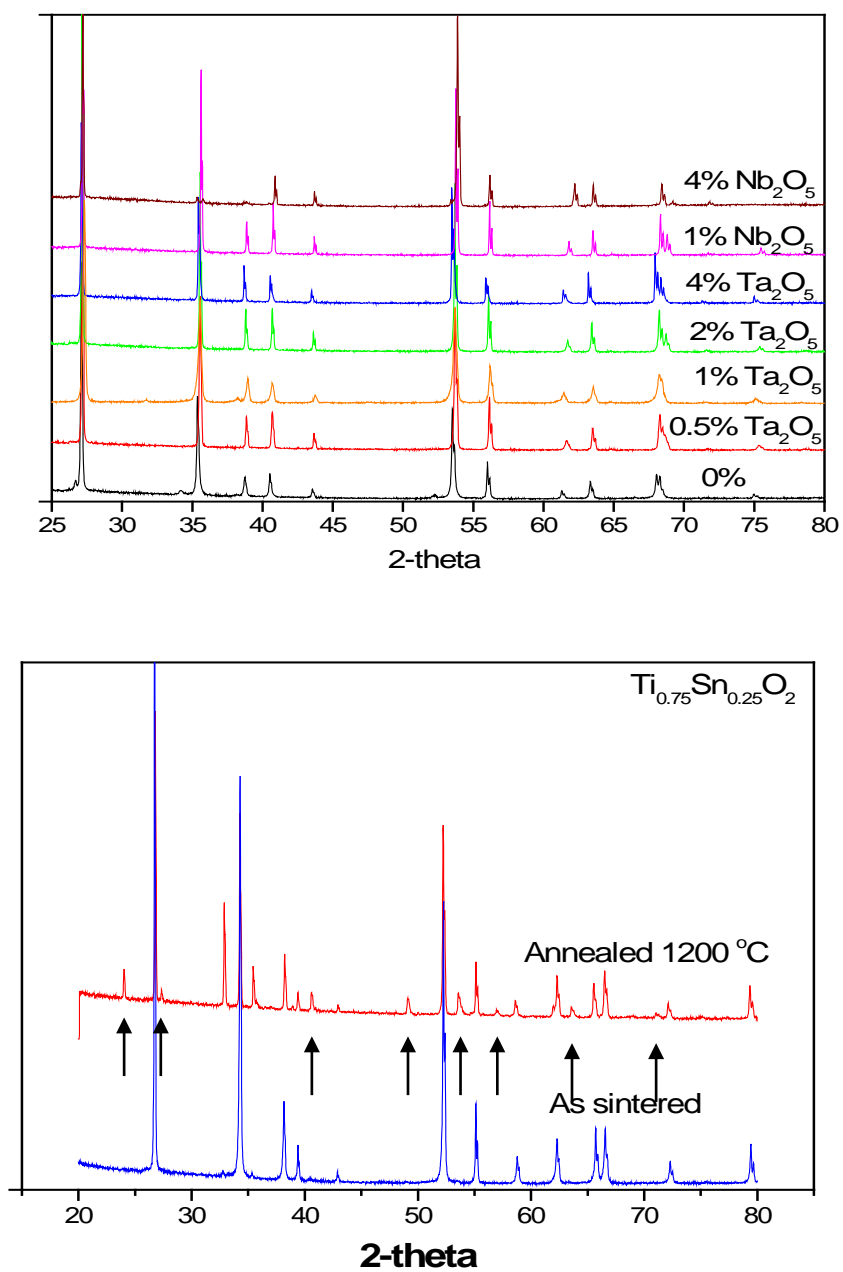


Fig. 4. A) XRD patterns of both undoped and doped $(\text{Ti}_{0.75}\text{Sn}_{0.25})\text{O}_2$ after sintering. B) XRD patterns for as-sintered and annealed $(\text{Ti}_{0.75}\text{Sn}_{0.25})\text{O}_2$. Arrows indicate new diffraction peaks.

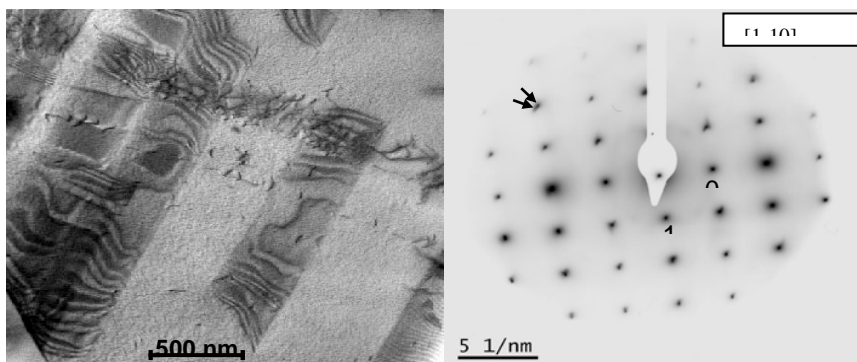


Fig. 5 Bright field image and SAD pattern of $(\text{Ti}_{0.75}\text{Sn}_{0.25})\text{O}_2$ doped with 1% Ta_2O_5 after sintering. Slightly misoriented domains are observed. The SAD does not show spot splitting along $[001]^*$ but small arcs around spots that reveal a small rotation along $[1-10]$.

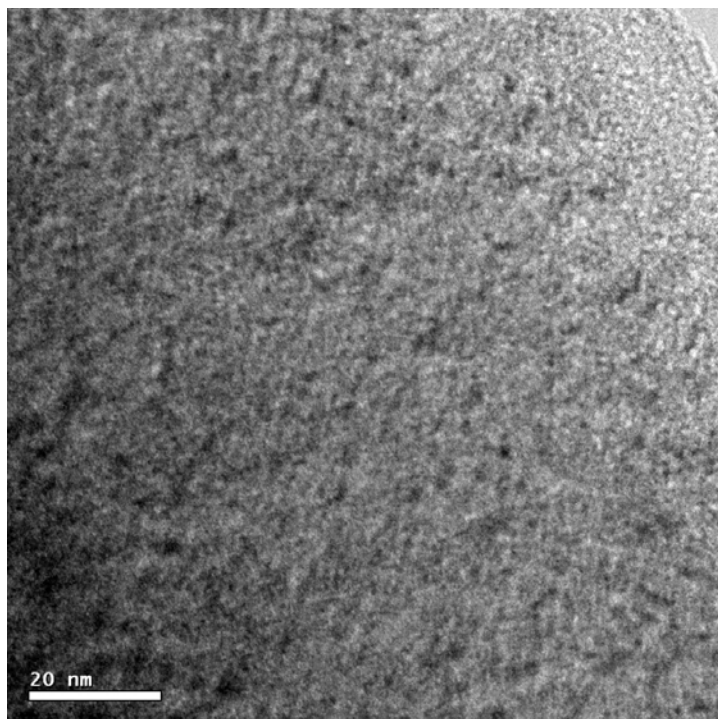


Fig. 6 Bright field image of a grain core in $(\text{Ti}_{0.75}\text{Sn}_{0.25})\text{O}_2$ doped with 1% Ta_2O_5 after sintering at 1500°C and annealing at 950°C in air for 48 hours. Intragranular dislocations are no longer visible. A tweed contrast is observed.

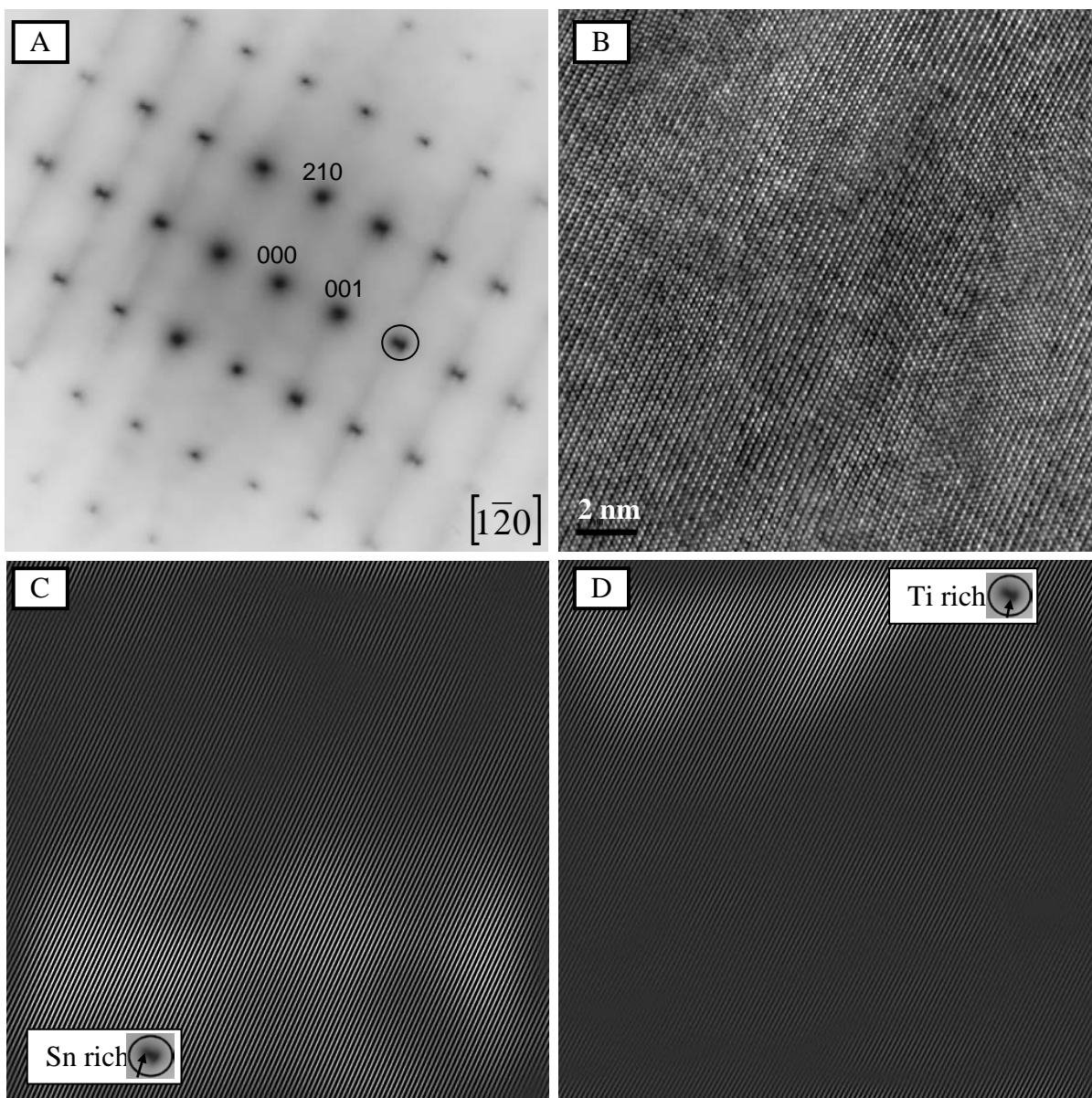


Fig. 7 $(\text{Ti}_{0.75}\text{Sn}_{0.25})\text{O}_2$ doped with 1% Ta_2O_5 after sintering at 1500°C and annealing at 950°C in air for 48 hours: A) SAD pattern in $[1\bar{2}0]$ zone axis showing a clear spot splitting along $[001]^*$ (circled on 002 spot), B) HRTEM image and C & D) inverse Fourier transforms on the two contributions to the 002 spot.

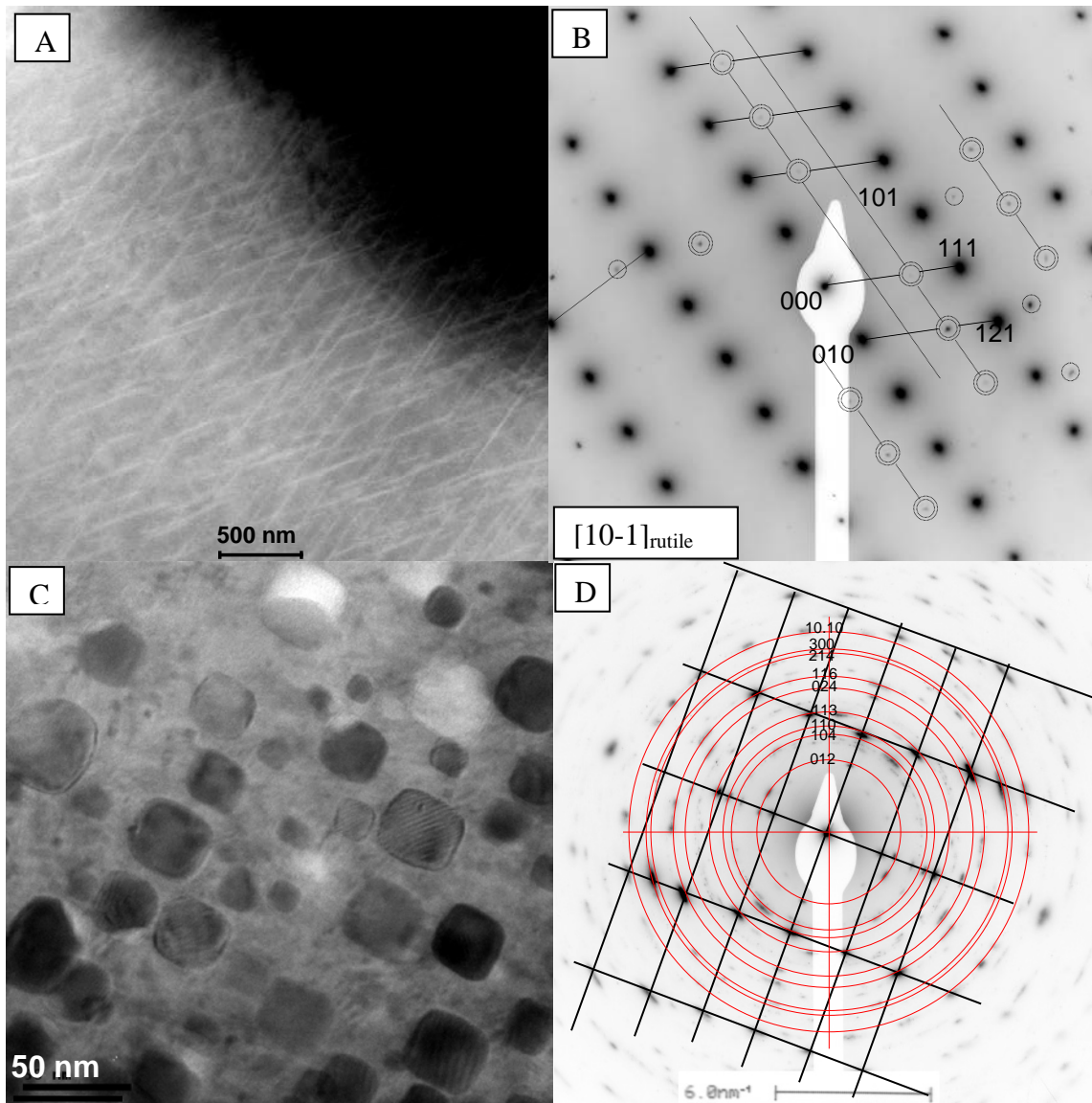


Fig. 8 Annealing at 1250°C produced a microstructure containing illmenite nano-precipitates in the rutile matrix: A) first stage of the nucleation, B) SAD pattern of first stage nucleation showing extra weak spots at $1/3$ and $2/3$ $[111]^*$; a few spots at almost $1/3$ and $2/3$ $[101]^*$, C) growth of illmenite (SnTiO_3) precipitates in a rutile matrix, and D) set of diffraction rings that can be indexed with both rutile and illmenite structure (only illmenite is shown for clarity). The lines refer to the rutile pattern in $[10-1]$ zone axis. The reinforcement of the rings around the corresponding nodes reveals the strong epitaxy relationship between precipitates and matrix.

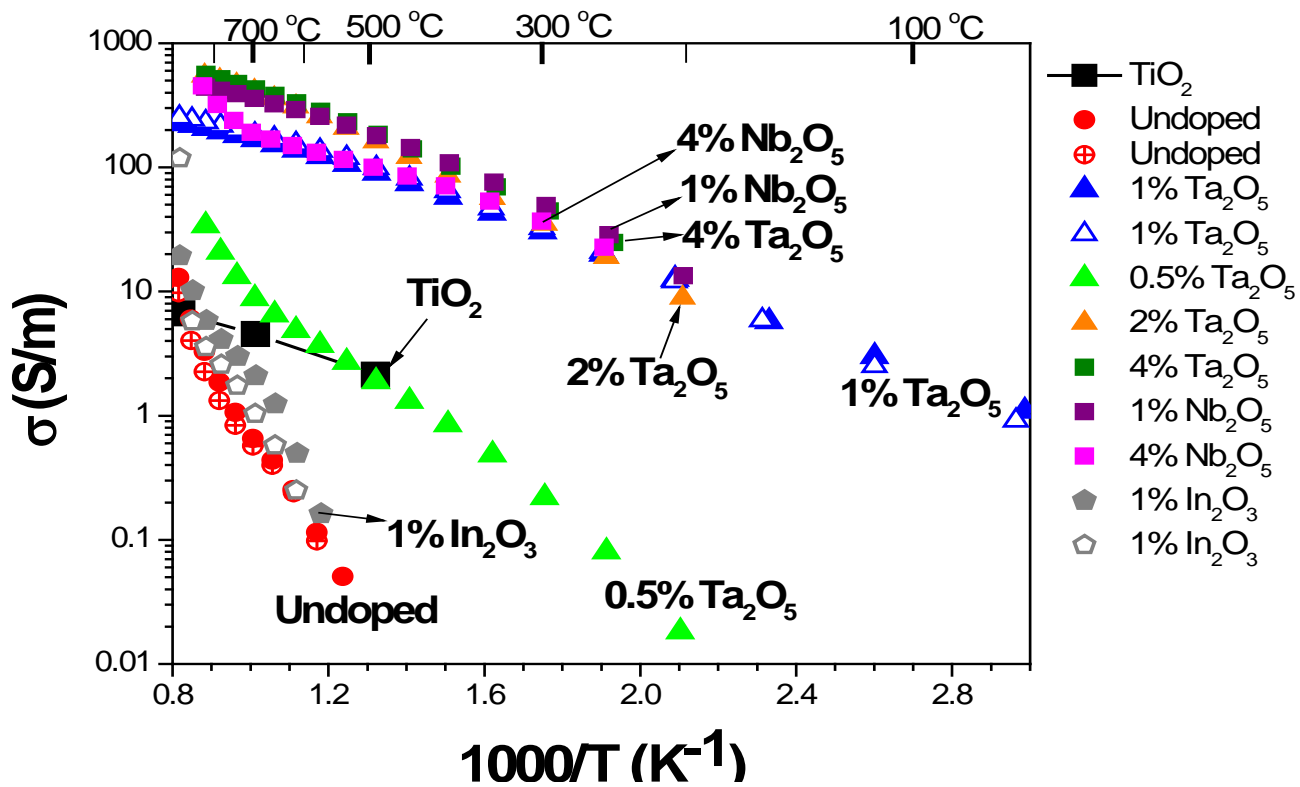


Fig. 9. Arrhenius plot of electrical conductivity of doped and undoped $(\text{Ti}_{0.75}\text{Sn}_{0.25})\text{O}_2$.

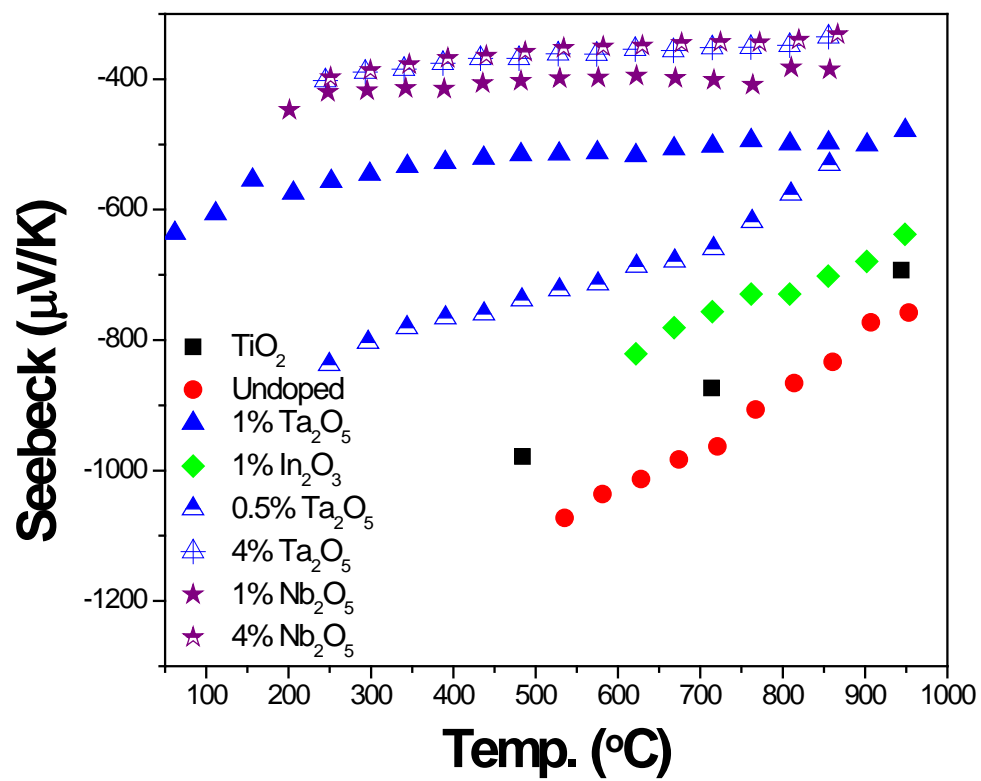


Fig. 10. Temperature dependent Seebeck coefficients of doped and undoped $(\text{Ti}_{0.75}\text{Sn}_{0.25})\text{O}_{2..}$

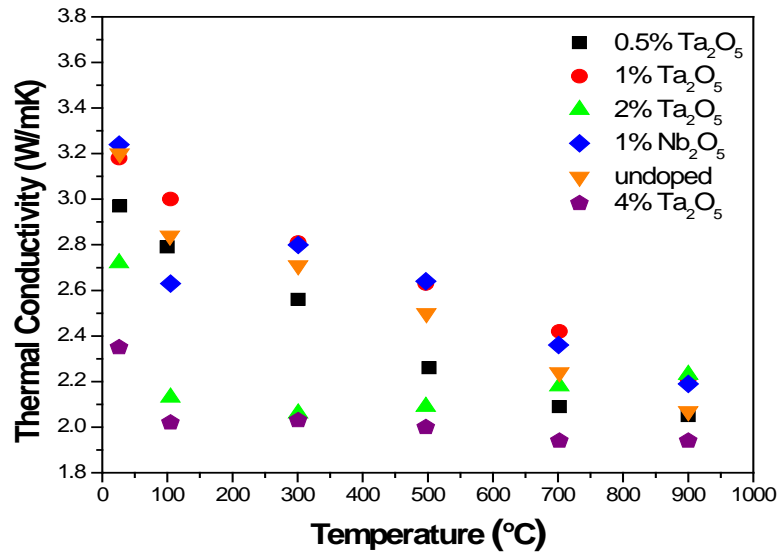
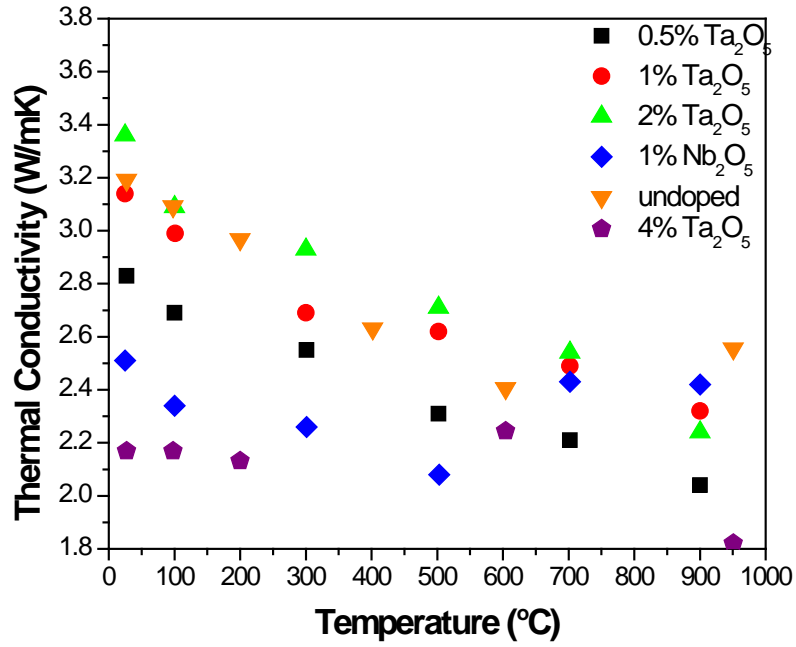


Fig. 11. Thermal conductivity of doped and undoped $(\text{Ti}_{0.75}\text{Sn}_{0.25})\text{O}_2$: (A) As sintered samples and (B) annealed at 1200 °C for 72 hrs in air.

References:

1. T. Itoh et al., "Large Thermoelectric Power in NaCo_2O_4 Single Crystals", *Phys. Rev. B*, **56**, 12685-12687, 1997.
2. H Ohta et al. "Giant thermoelectric Seebeck coefficient of a two-dimensional electron gas in SrTiO_3 ", *Nature Materials* **6**, 129 – 134, 2007.
3. H. Ohta et al. "Critical Thickness for Giant Thermoelectric Seebeck Coefficient of 2DEG confined in $\text{SrTiO}_3/\text{SrTi}_{0.8}\text{Nb}_{0.2}\text{O}_3$ Superlattices", *Thin Solid Films* **516**, 5916–5920, 2008.
4. D. Garica and D.H. Speidel, "System $\text{SnO}_2\text{-TiO}_2$ ", *J. Am. Cer. Soc.* **55**, 322-322, 1972.
5. A. H. Schultz and V. S. Stubican, "Modulated Structures in the System $\text{TiO}_2\text{-SnO}_2$ ", *Philos. Mag.*, **18**, 929-937, 1968.
6. J. Takahashi et al., "Decomposition Behaviors of Dopant Free and Dopant Solid Solutions in the $\text{TiO}_2\text{-SnO}_2$ System", *J. Mat. Sci.* **23**, 337-342, 1988.
7. T.C. Yuan and V. Virkar, "Kinetics of Phase Transformation in the $\text{TiO}_2\text{-SnO}_2$ System Outside the Coherent Spinodal: Role of Aliovalent Dopants", *J. Am. Cer. Soc.*, **69**, C310-C312, 1986.
8. T.C. Yuan and V. Virkar, "Kinetics of Spinodal Decomposition in the $\text{TiO}_2\text{-SnO}_2$ System Outside the Coherent Spinodal: The Effect of Aliovalent Dopants", *J. Am. Cer. Soc.*, **71**, 12-21, 1988.
9. M. W. Park et al., "Decomposition of $\text{TiO}_2\text{-SnO}_2$ Solid Solutions", *J. Mat. Sci.* **23**, 1227-1238, 1976.
10. J.F. Banfield, D.R. Veblen "The Structure and Origin of Fe-bearing Platelets in Metamorphic Rutile" *Am. Miner.* **76**, 113-127, 1991.
11. H.V. Yu and P. Shen "Phase transformations and microstructures of $\text{TiO}_2\text{-SnO}_2$ due to solution annealing versus reactive sintering" *J. Europ. Cer. Soc.* **28**, 91-99, 2008.
12. D.H. Zong and H.L. Ma, "Scattering Mechanisms of Charge Carriers in Transparent Conducting Oxide Films", *Appl. Phys. A*, **62**, 487-492, 1996.
13. P.R. Bueno et al., "Sintering and Mass Transport Features of $(\text{Sn,Ti})\text{O}_2$ Polycrystalline Ceramics" *J. Europ. Cer. Soc.* **22**, 887-896, 2003.
14. K.C. Yang and P. Shen, "On the Precipitation of Coherent Spinel Nanoparticles in Ti-Doped MgO " *J. Solid State Chem.* **178**, 661–670, 2005.
15. The Defect Chemistry of Metal Oxides, D. M. Smyth, Oxford Univ. Press, New York, 2000.
16. P.R. Bueno et al., "Low-Voltage Varistor Based on $(\text{Sn,Ti})\text{O}_2$ Ceramics" *J. Am. Ceram. Soc.* **85**, 282–284, 2002.
17. R.R. Heikes, Thermoelectricity ~Interscience, New York, 1961! Thermoelectricity: science and engineering [[by] Robert R. Heikes and Roland W. Ure, Jr New York, Interscience Publishers, 1961.
18. Electronic Conduction in Oxides, N. Tsuda et al., Springer, New York, 2000.
19. J. Nowotny et al., "Semiconducting Properties of undoped TiO_2 " *J. Phys. Chem Solids* Vol58, No. 6, pp. 927-937, 1997
20. M. Radecka et al., "Transport properties of $(\text{Sn,Ti})\text{O}_2$ polycrystalline ceramics and thin films" *Solid State Ionic*, **119**, 43–48, 1999.
21. V.C. Sousa et al., "Effect of Atmosphere on the electrical properties of $\text{TiO}_2\text{-SnO}_2$ Varistor Systems", *J. Mat. Sci.:Materials in Electronics*, **15**, 665-669, 2004.

22. B. Poumellec et al., "Electron Transport in $\text{Ti}_{1-x}\text{Nb}_x\text{O}_2$ Solid Solutions with $x < 4\%$ ", *J. Phys. Chem. Solids*, 41, 381-385, 1986.
23. B. Poumellec and J. F. Marucco, "Electron Transport in $\text{Ti}_{1-x}\text{Nb}_x\text{O}_2$ Solid Solutions with $0.04 < x < 1$ " *J. Phys. Chem. Solids*, 46, 71-77, 1985.
24. M. H. Brooks, "Thermoelectric Materials", U.S. Navy Final Report, Contract No. NObs 78376, 1/31/1963.